J. Fluid Mech. (2022), *vol*. 936, A20, doi:10.1017/jfm.2022.60

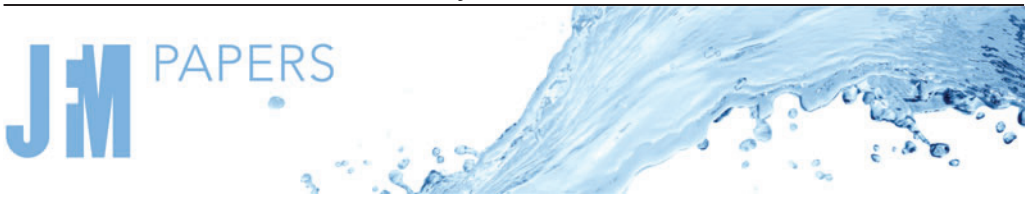

On diffraction and oblique interactions of horizontally two-dimensional internal solitary waves

Chunxin Yuan[1] **and Zhan Wang**[2,3,4,†]

[1]School of Mathematical Sciences, Ocean University of China, Qingdao 266100, PR China

[2]Institute of Mechanics, Chinese Academy of Sciences, Beijing 100190, PR China

[3]School of Engineering Science, University of Chinese Academy of Sciences, Beijing 100049, PR China

[4]School of Future Technology, University of Chinese Academy of Sciences, Beijing 100049, PR China

(Received 22 July 2021; revised 2 January 2022; accepted 15 January 2022)

In the context of three-dimensional oceanic internal waves, taking topographic effects into account, a modified Benney–Luke equation is proposed for describing internal wave–wave interactions on a sloping bottom. The derived equation is characterised by isotropy and bi-directional propagation, which are absent in the widely used Kadomtsev–Petviashvili equation. Indeed, these disparities are confirmed by numerical results of the diffraction of a truncated internal solitary wave and the evolution of a partially bent solitary wave. However, a good agreement between the numerical results of the modified Benney–Luke equation and those of the primitive equations confirms the validity of our simplified model. Because the stratification in a realistic ocean environment is usually continuous, in contrast to the assumption of a sharp density discontinuity used here, to maintain the kinematical equivalence, a layering scheme for determining the density and thickness of each layer from a continuous stratification is proposed. In addition, the occasionally observed but rarely examined X-shaped internal wave–wave interactions are shown to feature novel wave patterns, where topographic effects modulate the propagation speed, amplitude and waveform.

Key words: internal waves, solitary waves

1. Introduction

Internal waves play an important role in the Earth's climate system because these waves contribute to the global ocean transport and dissipation, which are vital to maintaining oceanic flows such as the meridional overturning circulation (Wunsch & Ferrari 2004).

† Email address for correspondence: zwang@imech.ac.cn

© The Author(s), 2022. Published by Cambridge University Press

https://doi.org/10.1017/jfm.2022.60 Published online by Cambridge University Press

In addition, these waves, especially large-amplitude internal solitary waves, usually induce turbulence at wave breaking and strong shear currents in areas they pass through and thus impact the marine ecosystem, offshore engineering and military applications like submarine navigation and detection. Internal waves have been observed in numerous sites around the world's coastal ocean. It is generally accepted that one of the significant generation mechanisms of these waves arises from barotropic tidal or other currents flowing over topography in the stratified ocean. From the place of generation, internal waves can propagate several hundred kilometres towards the continental shelf. During these long-distance travels, various factors, including (among others) variable topography, background currents and the Earth's rotation, can modulate the waveform leading to distinct wave patterns.

Theoretical analysis is one of the most important means of investigating internal solitary waves. However, most theoretical studies are based on horizontally one-dimensional models, such as the celebrated Korteweg–de Vries (KdV) equation and its numerous variants, the Benjamin–Ono (BO) equation, and the Miyata–Choi–Camassa (MCC) equation (the interested readers are referred to Helfrich & Melville (2006), Choi & Camassa (1996, 1999), Camassa *et al.* (2006) for more details). These models are reasonable, at least when the attention is focussed on a section plane that is generally far from the boundary or insensitive to the input from the boundary. Nevertheless, this is not appropriate for some general cases, for instance, when the interested region is too large to ignore three-dimensional effects.

For the study of horizontally two-dimensional internal waves, the Kadomtsev–Petviashvili (KP) equation (Kadomtsev & Petviashvili 1970), which is a generalisation of the KdV equation featuring uni-directional wave propagation with slight inhomogeneity in the transverse direction, has mostly been implemented (see, for example, Grimshaw & Melville 1989; Pierini 1989; Chen & Philip 1995; Yuan *et al.* 2018*a*,*b*). In addition, the KP equation, generally in a succinct form, has been extensively investigated from a rigorous mathematical point of view (see Biondini & Pelinovsky (2008) and references therein), which facilitates the understanding of the dynamics of weakly nonlinear free-surface/internal waves in the long-wave approximation. While anisotropic uni-directional models have been successful in many aspects of the water wave problems, there are still some limitations. They cannot correctly describe the two-way propagation of water waves, such as wave reflection/transmission at seamounts and head-on collisions of solitary waves. Additionally, it is not suitable to use an anisotropic model to study wave phenomena whose transverse variations are similar to those in the primary direction of propagation. To overcome these shortcomings as well as afford a significant simplification over the primitive equations, Yuan, Wang & Chen (2020) recently modified the classic Benney–Luke equation that is both isotropic and bi-directional (Benney & Luke 1964) to make it applicable to internal waves. In their paper, however, the derived equation can only model the wave generation process and not the effects of topography on the propagation of internal waves, which is the primary concern of the present paper.

On the ocean surface, a striking feature of two-space-dimensional nonlinear waves is the oblique interactions of line solitons in the shallow water regime that form X, Y and more complex wave patterns, as shown, for instance, in photos taken by Ablowitz & Baldwin (2012) and in laboratory experiments conducted by Li, Yeh & Kodama (2011) and Yeh & Li (2014). These distinctive wave patterns are persistent in nature and can be qualitatively understood by solving the KP equation for interacting line solitons (Ablowitz & Baldwin 2012). By applying an inverse scattering method, Zakharov & Shabat (1974) first found an exact N-soliton solution to the KP equation describing multiple collisions of solitons

https://doi.org/10.1017/jfm.2022.60 Published online by Cambridge University Press

with different propagation directions. Inspired by the experimental reflection patterns of surface solitary waves with oblique incidence along a vertical wall reported by Perroud (1957), Miles (1977*a*,*b*) originally linked the Y-shaped interaction with the KP equation as well as with the Mach stem phenomenon in gas dynamics. Both water tank experiments (Melville 1980) and numerical simulations (Funakoshi 1980) were conducted to validate Miles' theory. With the aid of more advanced instruments and techniques, Li *et al.* (2011) found that the evolution of stem-wave amplification is in good agreement with the KP theory, and the asymptotic characteristics and behaviours agree well with the theory of Miles (1977*b*) in the region away from the transition between regular reflection and Mach reflection. Based on a high-order spectral model, Tanaka (1993) illustrated that the effect of large amplitude tends to suppress the Mach reflection, and the theoretical predictions of Johnson (1982) exhibit better agreement than those of Miles for sufficiently small angles. In Tanaka's simulations, the 'four-fold amplification' was not observed, and this point was underscored by a recent work of Nakayama, Kakinuma & Tsuji (2019) using a fully nonlinear, strongly dispersive internal wave model. These research findings naturally lead us to contemplate the oblique interactions of internal solitary waves, which have been recorded by satellite images in Xue *et al.* (2014). Nonetheless, studies concentrated on this topic are still rare, although Yuan *et al.* (2018*a*) investigated one scenario where the initial wave was composed of two interacting internal solitons forming a V-shaped pattern.

In the current work, we focus on oblique interactions of internal solitary waves based on an isotropic bi-directional model, namely the modified Benney–Luke (mBL) equation. The problem is idealised as the wave propagation on the sharp density discontinuity between immiscible fluids in a two-layer system with the 'rigid lid' approximation and uneven bottom topography. In the long-wave approximation (the thickness of both layers are small compared with the characteristic wavelength), a Benney–Luke-type equation can be derived from the primitive equations in the Hamiltonian framework with the aid of the Dirichlet–Neumann operators and their asymptotic expansions (see § 2). Because a general analytical solution is difficult to obtain for the mBL equation, numerical simulations are implemented in § 3 via a Fourier pseudo-spectral scheme together with the method of integrating factors. In addition, a special windowing method for tackling the boundary conditions is also introduced. Although, in theory, the mBL equation possesses an advantage over the KP equation in some scenarios, the evidence has rarely been shown in previous works. Thus, we illustrate in § 4 disparities between these two equations with examples of the diffraction of a truncated solitary wave and the evolution of a partially bent solitary wave. More importantly, in these two examples, numerical results of the mBL equation show good agreement with direct numerical simulations of the primitive equations, further confirming the validity of the mBL equation. Then, oblique interactions between internal line solitary waves are thoroughly investigated by taking the X-shaped wave pattern as the initial condition, where the topographic effects are also considered. Finally, concluding remarks are given in § 5.

2. Derivation

2.1. *Model set-up*

Consider a three-dimensional incompressible and inviscid fluid system composed of two immiscible and homogeneous layers on top of each other. We denote by $\rho^{\pm}$ the density in each layer, where the superscripts '+' and '−' refer to fluid properties associated with the upper and lower fluid layers, respectively. Two fluids are separated by a sharp interface $z = \eta(x, y, t)$, where x and y are horizontal coordinates, and the z-axis points upwards

https://doi.org/10.1017/jfm.2022.60 Published online by Cambridge University Press

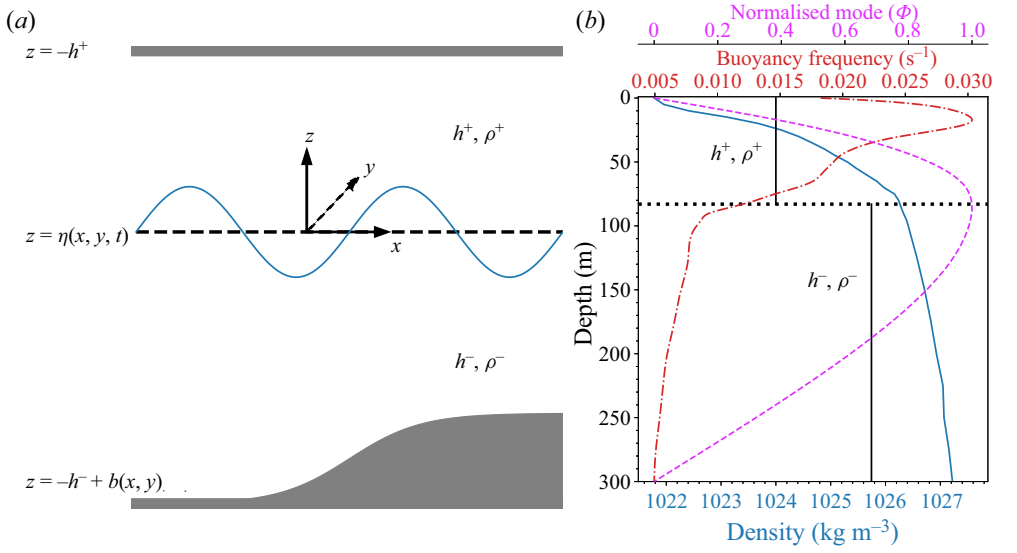

Figure 1. (*a*) Coordinate system and schematic of a two-fluid system characterized by densities $\rho^{\pm}$, thicknesses $h^{\pm}$ and bottom topography $b(x, y)$. (*b*) A continuous stratification with the density $\rho_0(z)$ (solid blue line), buoyancy frequency $N(z)$ (dash-dotted red line), normalised mode Φ (dashed cyan line) and its kinematically equivalent two-layer division obtained by implementing the layering scheme proposed in § 4.1 to the continuous stratification. The densities $\rho^{\pm}$ and depths $h^{\pm}$ for the two-layer system are chosen rationally, namely via matching the primary parameters of the KP equation derived based on the density-discontinuity system with those of the KP equation associated with the known continuous stratification (see details in § 4.1).

with $z = 0$ the undisturbed interface. The upper layer is bounded above by a rigid lid at $z = h^+$, and the lower layer is bounded below by a variable bottom $z = -h^- + b(x, y)$ where $b(x, y)$ is a prescribed function (see figure 1 for the coordinate system and layering). The system is in a stable density configuration, i.e. $\rho^+ < \rho^-$, and, given the length scale of internal oceanic waves, the effect of the interfacial tension can be neglected. The flow in each layer is supposed to be irrotational so that velocity potentials $\phi^{\pm}$ can be introduced, satisfying the Laplace equation in respective domains, namely

$$\left.\begin{aligned} \Delta\phi^- + \phi^-_{zz} = 0 \quad \text{for } -h^- + b(x, y) < z < \eta(x, y, t), \\ \Delta\phi^+ + \phi^+_{zz} = 0 \quad \text{for } \eta(x, y, t) < z < h^+, \end{aligned}\right\} \tag{2.1}$$

where Δ is the horizontal Laplace operator. At the interface $z = \eta(x, y, t)$, the nonlinear kinematic and dynamic boundary conditions read

$$\eta_t = \phi^-_z - \nabla\phi^- \cdot \nabla\eta = \phi^+_z - \nabla\phi^+ \cdot \nabla\eta \tag{2.2}$$

and

$$\rho^- \left[\phi^-_t + \tfrac{1}{2}\left|\nabla\phi^-\right|^2 + \tfrac{1}{2}\left(\phi^-_z\right)^2 + g\eta\right] = \rho^+ \left[\phi^+_t + \tfrac{1}{2}\left|\nabla\phi^+\right|^2 + \tfrac{1}{2}\left(\phi^+_z\right)^2 + g\eta\right], \tag{2.3}$$

where ∇ and $\nabla\cdot$ are the horizontal gradient and divergent operators, respectively, and g is the acceleration owing to gravity. The kinematic boundary condition (2.2) implies that the

https://doi.org/10.1017/jfm.2022.60 Published online by Cambridge University Press

normal velocity is continuous across the interface

$$\left(\phi_x^-, \phi_y^-, \phi_z^-\right) \cdot \boldsymbol{n} = \left(\phi_x^+, \phi_y^+, \phi_z^+\right) \cdot \boldsymbol{n}, \tag{2.4}$$

where $\boldsymbol{n} = (-\eta_x, -\eta_y, 1)/\sqrt{1+|\nabla\eta|^2}$ is the unit normal vector on the interface pointing upwards. Finally, the impermeability boundary conditions,

$$\left.\begin{aligned} \phi_z^+ &= 0 \quad \text{at } z = h^+, \\ \phi_z^- - \nabla b \cdot \nabla\phi^- &= 0 \quad \text{at } z = -h^- + b(x,y), \end{aligned}\right\} \tag{2.5}$$

complete the whole system.

2.2. *Hamiltonian and truncation*

It is well known that the two-layer interfacial wave problem has a Hamiltonian structure (Benjamin & Bridges 1997), and the Hamiltonian functional is the total energy:

$$\begin{aligned} \mathcal{H}\left[\phi^{\pm}, \eta\right] = {} & \frac{1}{2}\int_{\mathbb{R}^2}\int_{-h^-+b}^{\eta}\left[\left|\nabla\phi^-\right|^2 + \left(\phi_z^-\right)^2\right]\mathrm{d}z\,\mathrm{d}x\,\mathrm{d}y \\ & + \frac{R}{2}\int_{\mathbb{R}^2}\int_{\eta}^{h^+}\left[\left|\nabla\phi^+\right|^2 + \left(\phi_z^+\right)^2\right]\mathrm{d}z\,\mathrm{d}x\,\mathrm{d}y + \frac{1-R}{2}\int_{\mathbb{R}^2} g\eta^2\,\mathrm{d}x\,\mathrm{d}y, \end{aligned} \tag{2.6}$$

where $R = \rho^+/\rho^-$ is the ratio of the upper to lower density. The most important term in the Hamiltonian formulation is the Dirichlet–Neumann operator which maps the Dirichlet boundary condition to normal derivatives by solving the Laplace equation. If we denote by $\xi^{\pm}(x,y,t) = \phi^{\pm}(x,y,\eta(x,y,t),t)$ the velocity potentials at the interface, then the Dirichlet–Neumann operators, $G^{\pm}$, which are associated with kinematic boundary conditions, can be defined as

$$\eta_t = G^-(\eta, h^-, b)\xi^- = \left(\phi_x^-, \phi_y^-, \phi_z^-\right) \cdot \boldsymbol{n}\sqrt{1+|\nabla\eta|^2}, \tag{2.7}$$

$$\eta_t = -G^+(\eta, h^+)\xi^+ = -\left(\phi_x^+, \phi_y^+, \phi_z^+\right) \cdot (-\boldsymbol{n})\sqrt{1+|\nabla\eta|^2}. \tag{2.8}$$

Introducing a new variable $\xi = \xi^- - R\xi^+$, it follows from (2.7)–(2.8) that

$$\xi^+ = -\left(G^+ + RG^-\right)^{-1} G^-\xi, \quad \xi^- = \left(G^+ + RG^-\right)^{-1} G^+\xi, \tag{2.9a,b}$$

where we suppress the dependence of $G^{\pm}$ on η, $h^{\pm}$ and b for simplicity of notations. Using the divergence theorem and (2.9*a*,*b*), one can rewrite the Hamiltonian (2.6) in terms of ξ and η as

$$\mathcal{H}\left[\xi, \eta\right] = \frac{1}{2}\int_{\mathbb{R}^2} \xi G^-\left(G^+ + RG^-\right)^{-1} G^+\xi\,\mathrm{d}x\,\mathrm{d}y + \frac{1-R}{2}\int_{\mathbb{R}^2} g\eta^2\,\mathrm{d}x\,\mathrm{d}y. \tag{2.10}$$

It was first proved by Benjamin & Bridges (1997) that η and ξ constitute a pair of canonically conjugate variables, namely

$$\eta_t = \frac{\delta\mathcal{H}}{\delta\xi}, \quad \xi_t = -\frac{\delta\mathcal{H}}{\delta\eta}. \tag{2.11a,b}$$

It is well known that for the case of a flat bottom, if the C^1-norm of η is smaller than a certain constant, then $G^{\pm}$ are analytic functions of η (see, for example Craig, Schanz

https://doi.org/10.1017/jfm.2022.60 Published online by Cambridge University Press

& Sulem 1997). It directly follows that $G^{\pm}$ can be naturally written in the form of convergent Taylor series expansions $G^{\pm} = \sum_{n=0}^{\infty} G_n^{\pm}$ with the recursion formulae $G_n^{\pm}$ being homogeneous of order n in η. While for an uneven bottom, the expansion was extended by Craig *et al.* (2005) and Guyenne & Nicholls (2008), who showed that it was in the form of a double series in $b(x, y)$ and $\eta(x, y, t)$. We list below the first several terms of the Taylor series, which are sufficient for our derivation, and the interested readers are referred to the aforementioned references for the complete recursive formulae. For the lower half-plane, the first three terms of the Taylor series are given by

$$\left.\begin{aligned} G_0^- &= |D|\tanh\left(h^-|D|\right) + \operatorname{sech}\left(h^-|D|\right)\sum_{j=1}^{\infty}|D|\mathcal{L}_j(h^-, b),\\ G_1^- &= -G_0^-\eta G_0^- - \nabla\cdot\eta\nabla,\\ G_2^- &= \tfrac{1}{2}\Delta\eta^2 G_0^- + \tfrac{1}{2}G_0^-\eta^2\Delta + G_0^-\eta G_0^-\eta G_0^-, \end{aligned}\right\} \tag{2.12}$$

where $D = -\mathrm{i}\nabla$ and the pseudo-differential operator $|D|\mathcal{L}_j(h^-, b)$ for $j = 1, 2$ can be expressed as

$$\left.\begin{aligned} |D|\mathcal{L}_1 &= -D\cdot b\operatorname{sech}\left(h^-|D|\right)D,\\ |D|\mathcal{L}_2 &= D\cdot b\tanh\left(h^-|D|\right)|D|^{-1}DD\cdot b\operatorname{sech}\left(h^-|D|\right)D. \end{aligned}\right\} \tag{2.13}$$

For the upper layer, the first three terms in the Taylor series are given by

$$\left.\begin{aligned} G_0^+ &= |D|\tanh\left(h^+|D|\right),\\ G_1^+ &= G_0^+\eta G_0^+ + \nabla\cdot\eta\nabla,\\ G_2^+ &= \tfrac{1}{2}\Delta\eta^2 G_0^+ + \tfrac{1}{2}G_0^+\eta^2\Delta + G_0^+\eta G_0^+\eta G_0^+. \end{aligned}\right\} \tag{2.14}$$

The key point for deriving reduced model equations is to expand the pseudo-differential operator closely related to the kinetic energy in the Hamiltonian (2.10) in terms of some small parameters. In the subsequent analyses, we derive weakly nonlinear models in a classical long-wave scaling regime, namely the Boussinesq scaling. Suppose h^- and h^+ are of the same order. In that case, the long-wave regime is characterised by $a/h^{\pm}$ and $h^{\pm}/\lambda$, two parameters measuring nonlinearity and dispersion, respectively, where a is a typical wave amplitude and λ is a characteristic wavelength. The Boussinesq scaling enforces a balance between nonlinearity and dispersion by specifying $a/h^{\pm} = O(\epsilon^2)$ and $h^{\pm}/\lambda = O(\epsilon)$, where ϵ is taken to be a small parameter. To continue the derivation, we introduce new independent and dependent variables:

$$\tilde{x} = \epsilon x, \quad \tilde{y} = \epsilon y, \quad \tilde{t} = \epsilon t, \quad \tilde{\xi} = \frac{\xi}{\epsilon}, \quad \tilde{\eta} = \frac{\eta}{\epsilon^2}, \quad \tilde{b} = \frac{b}{\epsilon^2}. \tag{2.15a–f}$$

A straightforward calculation yields

$$G^- = -\epsilon^2 h^-\tilde{\Delta} - \epsilon^4\frac{(h^-)^3}{3}\tilde{\Delta}^2 + \epsilon^4\tilde{\nabla}\cdot\tilde{b}\tilde{\nabla} - \epsilon^4\tilde{\nabla}\cdot\tilde{\eta}\tilde{\nabla} + O\left(\epsilon^6\right), \tag{2.16}$$

$$G^+ = -\epsilon^2 h^+\tilde{\Delta} - \epsilon^4\frac{(h^+)^3}{3}\tilde{\Delta}^2 + \epsilon^4\tilde{\nabla}\cdot\tilde{\eta}\tilde{\nabla} + O\left(\epsilon^6\right), \tag{2.17}$$

https://doi.org/10.1017/jfm.2022.60 Published online by Cambridge University Press

where $\tilde{\boldsymbol{\nabla}} = (\partial_{\tilde{x}}, \partial_{\tilde{y}})$ and $\tilde{\Delta} = \tilde{\boldsymbol{\nabla}} \cdot \tilde{\boldsymbol{\nabla}}$. It then follows that

$$\begin{aligned} & G^{-}\left(G^{+}+RG^{-}\right)^{-1}G^{+} \\ & \quad = \epsilon^{2}\frac{h^{-}h^{+}}{h^{+}+Rh^{-}}\tilde{\Delta} - \epsilon^{4}\frac{\left(h^{-}h^{+}\right)^{2}\left(h^{-}+Rh^{+}\right)}{3\left(h^{+}+Rh^{-}\right)^{2}}\tilde{\Delta}^{2} \\ & \quad + \epsilon^{4}\frac{R\left(h^{-}\right)^{2}-\left(h^{+}\right)^{2}}{\left(h^{+}+Rh^{-}\right)^{2}}\tilde{\boldsymbol{\nabla}}\cdot\tilde{\eta}\tilde{\boldsymbol{\nabla}} + \epsilon^{4}\frac{\left(h^{+}\right)^{2}}{\left(h^{+}+Rh^{-}\right)^{2}}\tilde{\boldsymbol{\nabla}}\cdot\tilde{b}\tilde{\boldsymbol{\nabla}} + O\left(\epsilon^{6}\right). \end{aligned} \tag{2.18}$$

Substituting (2.18) into (2.10), taking the variational derivatives as given in (2.11*a*,*b*), and retaining terms valid up to $O(\epsilon^2)$, one obtains

$$\begin{aligned} \tilde{\eta}_{\tilde{t}} = & -\frac{h^{-}h^{+}}{h^{+}+Rh^{-}}\tilde{\Delta}\tilde{\xi} - \epsilon^{2}\frac{\left(h^{-}h^{+}\right)^{2}\left(h^{-}+Rh^{+}\right)}{3\left(h^{+}+Rh^{-}\right)^{2}}\tilde{\Delta}^{2}\tilde{\xi} \\ & + \epsilon^{2}\frac{R\left(h^{-}\right)^{2}-\left(h^{+}\right)^{2}}{\left(h^{+}+Rh^{-}\right)^{2}}\tilde{\boldsymbol{\nabla}}\cdot\tilde{\eta}\tilde{\boldsymbol{\nabla}}\tilde{\xi} + \epsilon^{2}\frac{\left(h^{+}\right)^{2}}{\left(h^{+}+Rh^{-}\right)^{2}}\tilde{\boldsymbol{\nabla}}\cdot\tilde{b}\tilde{\boldsymbol{\nabla}}\tilde{\xi}, \end{aligned} \tag{2.19}$$

$$\tilde{\xi}_{\tilde{t}} = -(1-R)g\tilde{\eta} + \epsilon^{2}\frac{R\left(h^{-}\right)^{2}-\left(h^{+}\right)^{2}}{2\left(h^{+}+Rh^{-}\right)^{2}}\left|\tilde{\boldsymbol{\nabla}}\tilde{\xi}\right|^{2}, \tag{2.20}$$

a Boussinesq-type system for interfacial waves propagating on a variable topography. We next recast the system (2.19)–(2.20) to a single evolution equation describing bi-directional waves. Differentiating (2.20) with respect to the rescaled time $\tilde{t}$ yields

$$\tilde{\xi}_{\tilde{t}\tilde{t}} = -(1-R)g\tilde{\eta}_{\tilde{t}} + \epsilon^{2}\frac{R\left(h^{-}\right)^{2}-\left(h^{+}\right)^{2}}{2\left(h^{+}+Rh^{-}\right)^{2}}\left(\left|\tilde{\boldsymbol{\nabla}}\tilde{\xi}\right|^{2}\right)_{\tilde{t}}. \tag{2.21}$$

Substituting (2.19) into (2.21), eliminating $\tilde{\eta}$ by using the relation $\tilde{\xi}_{\tilde{t}} = -(1-R)g\tilde{\eta} + O(\epsilon^2)$ and retaining terms valid up to $O(\epsilon^2)$, one arrives at

$$\begin{aligned} \tilde{\xi}_{\tilde{t}\tilde{t}} - c^{2}\tilde{\Delta}\tilde{\xi} = & \epsilon^{2}\frac{(1-R)g\left(h^{-}h^{+}\right)^{2}\left(h^{-}+Rh^{+}\right)}{3\left(h^{+}+Rh^{-}\right)^{2}}\tilde{\Delta}^{2}\tilde{\xi} - \epsilon^{2}\frac{(1-R)g\left(h^{+}\right)^{2}}{\left(h^{+}+Rh^{-}\right)^{2}}\tilde{\boldsymbol{\nabla}}\cdot\tilde{b}\tilde{\boldsymbol{\nabla}}\tilde{\xi} \\ & + \epsilon^{2}\frac{R\left(h^{-}\right)^{2}-\left(h^{+}\right)^{2}}{\left(h^{+}+Rh^{-}\right)^{2}}\left[\left(\left|\tilde{\boldsymbol{\nabla}}\tilde{\xi}\right|^{2}\right)_{\tilde{t}} + \tilde{\xi}_{\tilde{t}}\tilde{\Delta}\tilde{\xi}\right], \end{aligned} \tag{2.22}$$

where the leading-order wave speed c is given by

$$c^{2} = \frac{(1-R)gh^{-}h^{+}}{h^{+}+Rh^{-}}. \tag{2.23}$$

As pointed out by Milewski & Tabak (1999), (2.22) is linearly ill-posed for short waves, and a regularisation is required, which can be achieved by replacing the linear dispersive

https://doi.org/10.1017/jfm.2022.60 Published online by Cambridge University Press

term $\tilde{\Delta}^2\tilde{\xi}$ with $\tilde{\Delta}\tilde{\xi}_{\tilde{t}\tilde{t}}/c^2$. Finally, returning to the original variables, (2.22) becomes

$$\xi_{tt} - c^2\Delta\xi - \alpha\Delta\xi_{tt} + \beta\nabla\cdot b\nabla\xi + \gamma\left[\left(|\nabla\xi|^2\right)_t + \xi_t\Delta\xi\right] = 0, \tag{2.24}$$

where

$$\alpha = \frac{h^-h^+\left(h^- + Rh^+\right)}{3\left(h^+ + Rh^-\right)}, \quad \beta = \frac{(1-R)g\left(h^+\right)^2}{\left(h^+ + Rh^-\right)^2}, \quad \gamma = \frac{\left(h^+\right)^2 - R\left(h^-\right)^2}{\left(h^+ + Rh^-\right)^2}. \tag{2.25a–c}$$

Equation (2.24) modifies the classic Benney–Luke equation to account for nonlinear internal waves propagating over variable bottom topography. Note that the modified Benney–Luke (mBL) equation embodies the characters of isotropy and bi-directional propagation, which are absent in the KP equation. However, in contrast to the Boussinesq-type equations, (2.24) admits an analytic solution for internal line solitary waves in the absence of topography, which can be explicitly expressed as

$$\xi_t = A(k)\,\mathrm{sech}^2(\boldsymbol{k}\cdot\boldsymbol{r} - vkt), \quad \xi = -\frac{A}{vk}\tanh(\boldsymbol{k}\cdot\boldsymbol{r} - vkt), \tag{2.26a,b}$$

where $\boldsymbol{r} = (x, y)$ is a vector in any direction on the horizontal plane, and $\boldsymbol{k} = (k_x, k_y)$ is the corresponding wavenumber vector with the magnitude of $k = \sqrt{k_x^2 + k_y^2}$. The amplitude $A(k)$ and nonlinear wave speed $v(k)$ take the forms

$$A(k) = -\frac{4\alpha v^2k^2}{\gamma}, \quad v^2 = \frac{c^2}{1 - 4\alpha k^2}. \tag{2.27a,b}$$

2.3. *Degeneration to the KP equation*

For the inhomogeneous case, where variation in the y-direction is much slower than in the x-direction, the mBL equation (2.24) can be reduced to the well-known KP equation. We introduce new variables

$$X = \tilde{x} - c\tilde{t}, \quad T = \epsilon^2\tilde{t}, \quad Y = \epsilon\tilde{y}, \tag{2.28a–c}$$

to focus upon the right-moving evolution and weak transverse variation. Letting $\Upsilon(X, Y, T) = \tilde{\xi}(\tilde{x}, \tilde{y}, \tilde{t})$, substituting

$$\partial_{\tilde{t}} = -c\partial_X + \epsilon^2\partial_T, \quad \partial_{\tilde{x}} = \partial_X, \quad \partial_{\tilde{y}} = \epsilon\partial_Y \tag{2.29a–c}$$

into (2.22) and retaining the leading order terms, one obtains

$$\Upsilon_{XT} + \frac{c}{2}\Upsilon_{YY} - \frac{(1-R)g\left(h^+\right)^2}{2c\left(h^+ + Rh^-\right)^2}(b\Upsilon_X)_X - \frac{3}{2}\frac{R\left(h^-\right)^2 - \left(h^+\right)^2}{\left(h^+ + Rh^-\right)^2}\Upsilon_X\Upsilon_{XX} + \frac{(1-R)g\left(h^-h^+\right)^2\left(h^- + Rh^+\right)}{6c\left(h^+ + Rh^-\right)^2}\Upsilon_{XXXX} = 0. \tag{2.30}$$

Upon noticing $\Upsilon_X = (g(1-R)/c)\tilde{\eta} + O(\epsilon^2)$, we get the KP equation in the original variables:

$$[\eta_t + c\eta_x + \varphi\eta\eta_x + \vartheta\eta_{xxx} - \zeta(b\eta)_x]_x + \frac{c}{2}\eta_{yy} = 0, \tag{2.31}$$

https://doi.org/10.1017/jfm.2022.60 Published online by Cambridge University Press

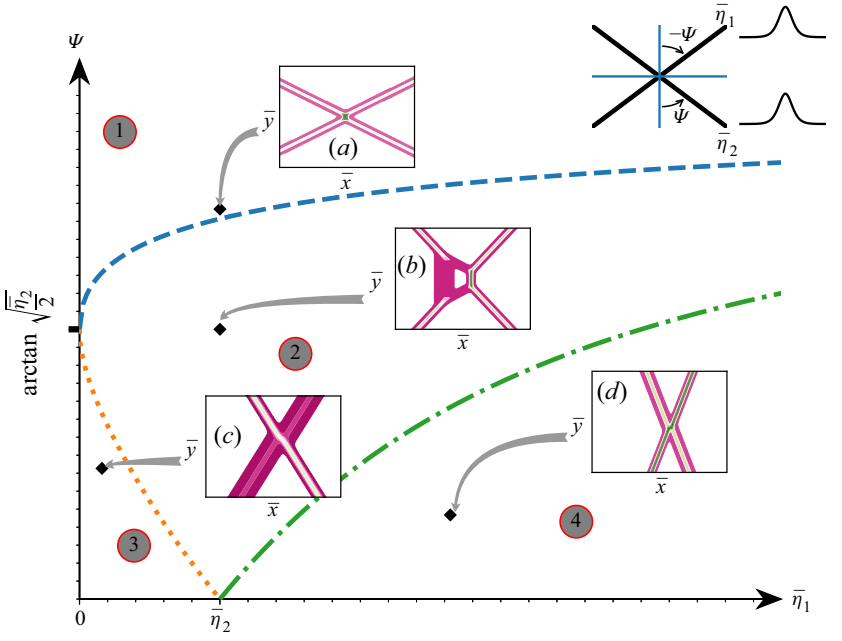

Figure 2. The initial X-shaped pattern, which is composed of two line solitons with amplitudes $\bar{\eta}_{1,2}$ and inclination angles $\pm\Psi$, is shown in the upper right corner. The $\bar{\eta}_1 - \Psi$ plane (for $\bar{\eta}_2$ fixed) can be divided into four regions according to evolution patterns of the KP equation which are shown in panels (*a*)–(*d*). The boundaries between different regions are given by $\sqrt{2\bar{\eta}_1} + \sqrt{2\bar{\eta}_2} = 2\tan\Psi$ (blue dashed line), $\sqrt{2\bar{\eta}_1} - \sqrt{2\bar{\eta}_2} = 2\tan\Psi$ (green dash–dotted line) and $\sqrt{2\bar{\eta}_2} - \sqrt{2\bar{\eta}_1} = 2\tan\Psi$ (orange dotted line). A similar figure plotted with other parameters can be found in Kao & Kodama (2012).

where

$$\varphi = \frac{3(1-R)g\left[\left(h^+\right)^2 - R\left(h^-\right)^2\right]}{2c\left(h^+ + Rh^-\right)^2}, \tag{2.32}$$

$$\vartheta = \frac{(1-R)g\left(h^-h^+\right)^2\left(h^- + Rh^+\right)}{6c\left(h^+ + Rh^-\right)^2}, \tag{2.33}$$

$$\zeta = \frac{(1-R)g\left(h^+\right)^2}{2c\left(h^+ + Rh^-\right)^2}. \tag{2.34}$$

The KP equation (2.31), in the absence of topography (i.e. $b = 0$), admits a line soliton

$$\eta = \eta_0 \operatorname{sech}^2\left[\Gamma\left(x + y\tan\Psi - \varpi t\right)\right], \tag{2.35}$$

where Ψ is the angle between the direction of soliton propagation and the y-axis (see the upper right diagram in figure 2), and the other parameters are given as

$$\Gamma = \sqrt{\frac{\varphi\eta_0}{12\vartheta}}, \quad \varpi = c\left(1 + \frac{\tan^2\Psi}{2}\right) + \frac{\varphi\eta_0}{3}, \quad \tan\Psi = \frac{k_y}{k_x}. \tag{2.36a–c}$$

https://doi.org/10.1017/jfm.2022.60 Published online by Cambridge University Press

3. Numerical method and boundary treatment

To study the evolution of internal solitary waves, in general, we have to solve the mBL equation numerically. Owing to the finiteness of the computational domain, the boundary condition needs special treatment in some cases to avoid radiated waves from re-entering the domain. For this purpose, a windowing method proposed by Schlatter, Adams & Kleiser (2005) will be used in the subsequent numerical experiments. Its core idea is to divide the solution domain into the interior and the boundary-layer regions in the transverse direction (orthogonal to wave propagation) using a smooth function with compact support, termed the window function. Because analytic solutions to the problem under investigation are usually used in the boundary layers, numerical errors inevitably emanate from junction regions and propagate inwards. However, as these tiny errors propagate with finite speed, little contamination affects the active portion of the wave phenomenon being studied if the domain is large enough considering our relatively short computation time.

We choose x as the direction of wave propagation and split the unknown ξ in (2.24) into two components:

$$\xi = \psi_1 + \psi_2 \quad \text{with } \psi_1 = W\xi, \quad \psi_2 = (1 - W)\xi. \tag{3.1}$$

The window function $W(y)$ is nearly one over some interval (say $[-L_y + \varepsilon, L_y - \varepsilon]$ for a small ε) and rapidly decays to zero near two boundaries $y = \pm L_y$. Specifically, $W(y)$ can be defined as

$$W(y) = \exp\left(-a\left|\frac{y}{L_y}\right|^n\right), \tag{3.2}$$

where $n = 95$ and $a = (1.02)^n \ln 10$ are chosen in all computations. It is clear that ψ_1 and ψ_2 represent the respective contributions of the interior and boundary-layer regions. Substituting (3.1) into (2.24) yields

$$\psi_{1tt} - c^2\Delta\psi_1 - \alpha\Delta\psi_{1tt} + \gamma\left[\left(|\nabla\psi_1|^2\right)_t + \psi_{1t}\Delta\psi_1\right] + \beta\nabla\cdot b\nabla\psi_1 = G_1 + G_2, \tag{3.3}$$

where

$$\left.\begin{aligned} G_1 &= \gamma\left[-2\nabla\psi_1\cdot\nabla\psi_{2t} - 2\nabla\psi_2\cdot\nabla\psi_{1t} - \psi_{1t}\Delta\psi_2 - \psi_{2t}\Delta\psi_1\right], \\ G_2 &= -\psi_{2tt} + c^2\Delta\psi_2 + \alpha\Delta\psi_{2tt} - \gamma\left[\left(|\nabla\psi_2|^2\right)_t + \psi_{2t}\Delta\psi_2\right] - \beta\nabla\cdot b\nabla\psi_2. \end{aligned}\right\} \tag{3.4}$$

In practice, the solution near the boundary is assumed to be a line solitary wave ξ_0 with the explicit expression (2.26*a*,*b*). Hence, $\psi_2 = (1 - W)\xi_0$ simplifies the computation of G_2. Thus, we can enforce doubly periodic boundary conditions for ψ_1, owing to its exponential decay in all spatial directions, and the pseudo-spectral method is applicable.

We next sketch the numerical scheme for time-dependent simulations of the mBL equation. Following Milewski & Tabak (1999), (3.3) can be rewritten as

$$(1 - \alpha\Delta)\psi_{1tt} - c^2\Delta\psi_1 = \mathcal{N}(\psi_{1,2}, \partial_t\psi_{1,2}, \nabla\psi_{1,2}, b), \tag{3.5}$$

where $\mathcal{N}$ includes all the nonlinear terms. Rearranging the operator $1 - \alpha\Delta$ and introducing

$$\theta = \left(\frac{\partial}{\partial t} + \mathrm{i}\mathcal{L}\right)\psi_1, \quad \mathcal{L}^2 = \frac{-c^2\Delta}{1 - \alpha\Delta}, \tag{3.6a,b}$$

https://doi.org/10.1017/jfm.2022.60 Published online by Cambridge University Press

(3.5) can be simplified to a complex first-order equation,

$$\left(\frac{\partial}{\partial t} - \mathrm{i}\mathcal{L}\right)\theta = \frac{1}{1-\alpha\Delta}\mathcal{N}(\psi_{1,2}, \partial_t\psi_{1,2}, \nabla\psi_{1,2}, b). \tag{3.7}$$

Taking the Fourier transform of the above equation in the spatial variables yields

$$\left(\frac{\partial}{\partial t} - \mathrm{i}\hat{\mathcal{L}}(\boldsymbol{k})\right)\hat{\theta}(\boldsymbol{k}, t) = \frac{\mathcal{F}\left[\mathcal{N}(\psi_{1,2}, \partial_t\psi_{1,2}, \nabla\psi_{1,2}, b)\right](\boldsymbol{k}, t)}{\mathcal{F}[1-\alpha\Delta](\boldsymbol{k})}, \tag{3.8}$$

where both $\hat{\cdot}$ and $\mathcal{F}$ stand for the Fourier transform and $\hat{\mathcal{L}}(\boldsymbol{k})$ is the Fourier symbol of the linear operator $\mathcal{L}$. The time-evolution equation (3.8) can be numerically advanced using the method of integrating factors coupled with the fourth-order Runge–Kutta scheme for time-stepping. Using the fact that ψ_1 is real, ψ_1 and $\partial_t\psi_1$ can be recovered from

$$\widehat{\psi_1}(\boldsymbol{k}, t) = \frac{\hat{\theta}(\boldsymbol{k}, t) - \hat{\theta}^*(-\boldsymbol{k}, t)}{\mathrm{i}\left[\hat{\mathcal{L}}(-\boldsymbol{k}) + \hat{\mathcal{L}}(\boldsymbol{k})\right]}, \tag{3.9}$$

$$\partial_t\widehat{\psi_1}(\boldsymbol{k}, t) = \frac{\hat{\theta}(\boldsymbol{k}, t) + \hat{\theta}^*(-\boldsymbol{k}, t)}{2}, \tag{3.10}$$

where the asterisk indicates complex conjugation. It should be pointed out that $\hat{\psi}_1(\boldsymbol{0}, t)$ cannot be recovered from (3.9) because $\hat{\mathcal{L}}(\boldsymbol{0}) = 0$, but instead, it should be updated numerically by integrating (3.10) at $\boldsymbol{k} = \boldsymbol{0}$. Finally, when internal solitary waves are chosen as initial conditions, the solution ξ given in (2.26*a*,*b*) is not a periodic function; therefore, modification is required. We replace ξ with

$$\xi = -\frac{A}{vk}\tanh(\boldsymbol{k}\cdot\boldsymbol{r} - vkt) + \boldsymbol{P}\cdot\boldsymbol{r}, \tag{3.11}$$

where $\boldsymbol{P}$ is a constant vector chosen to keep ξ periodic. In the following numerical simulations, dimensional variables are used to mimic the realistic oceanic environment. We pick 75 m as the spatial step in both x- and y-directions and 5 s as the temporal step in all computations.

4. Results

4.1. *Truncated and partially bent solitary waves*

In the ocean, one interesting scenario is the evolution of an internal solitary wave passing through a strait or diffracting off the end of a topographic feature; see those, for instance, in the Strait of Gibraltar (Vlasenko *et al.* 2009). We investigate this problem in the mBL equation and the KP equation, and the results are shown in panels (*b*) and (*e*) of figure 3, respectively. We take as initial data the solitary waves in the form of (2.26*a*,*b*) and (2.35) with amplitude of -20 m truncated at the ends with a fast cutoff (see figure 3*a*). In addition, the actual computational domain in the y-direction is twice as large as shown in the figure to allow for periodicity. A qualitative disparity can be found between these two models where a circular pattern emanates from the end of the truncated nonlinear wave in the mBL equation, compared with a bent dispersive wave in the KP equation. As shown in figure 3(*f*), the interface fluctuations at section lines $y = 0$ and 12.5 km also display differences. We claim that this comparison shows the advantage of the isotropic

https://doi.org/10.1017/jfm.2022.60 Published online by Cambridge University Press

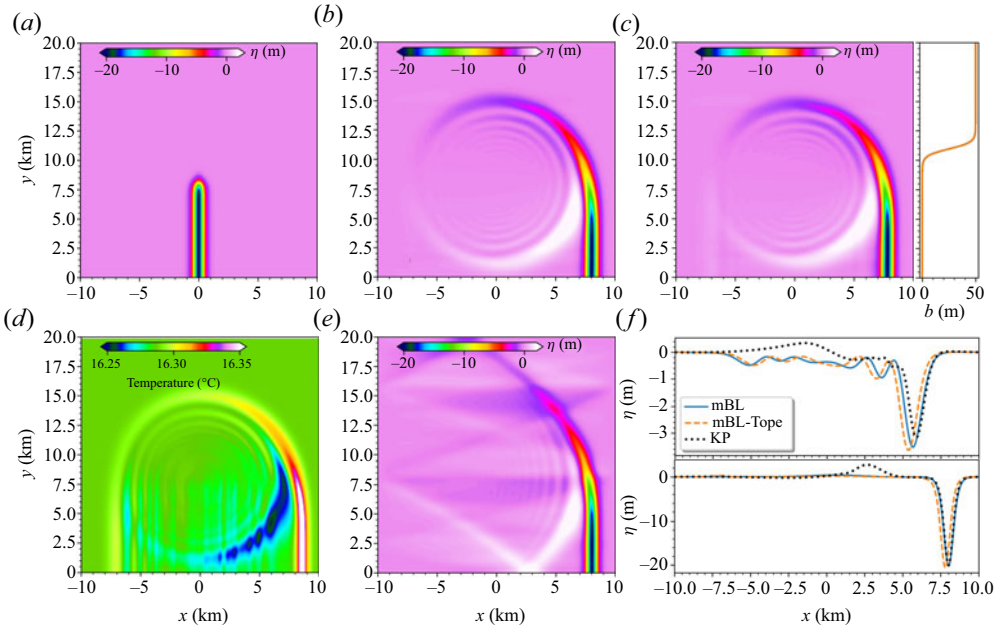

Figure 3. (*a*) Initial internal solitary wave of amplitude −20 m. (*b*) Snapshot of the wave pattern at $t = 7500$ s in the mBL equation with a flat bottom. (*c*) Snapshot of the wave pattern at $t = 7500$ s in the mBL equation in the presence of y-dependent topography $b(y)$ shown on the far right. (*d*) Temperature profile in the MITgcm model at $t = 7500$ s. (*e*) Snapshot of the wave pattern at $t = 7500$ s in the KP equation with a flat bottom. (*f*) Interface fluctuations along section lines $y = 0$ (bottom) and $y = 12.5$ km (top) at $t = 7500$ s.

bidirectional model. To put this assertion on a firmer footing and further verify the validity of the mBL equation, we conduct a numerical simulation with the same set-up based on the Massachusetts Institute of Technology general circulation model (MITgcm), which solves the fully nonlinear and non-hydrostatic primitive equations (see Marshall *et al.* (1997) for an overview of the MITgcm).

In the realistic situation, the ocean stratification is continuous; however, the mBL equation derived here is based on the two-layer simplification, which causes difficulty when it is intended to be invoked for the oceanic environment. We propose a layering scheme to establish a connection between continuous and discontinuous vertical density stratifications to circumvent this issue. Note that the KP equation (2.31) has an extension for a continuous stratification (see Yuan *et al.* (2018*b*) and the references therein), where, in the absence of topographic effects, the significant parameters are given as

$$I\varphi = 3\int_{-h^-}^{h^+} \rho_0 c^2 \Phi_z^3 \,\mathrm{d}z, \tag{4.1}$$

$$I\vartheta = \int_{-h^-}^{h^+} \rho_0 c^2 \Phi^2 \,\mathrm{d}z, \tag{4.2}$$

$$I = 2\int_{-h^-}^{h^+} \rho_0 c \Phi_z^2 \,\mathrm{d}z, \tag{4.3}$$

https://doi.org/10.1017/jfm.2022.60 Published online by Cambridge University Press

where $\rho_0(z)$ is the continuous density profile, and the mode Φ and linear phase speed c are obtained by solving the modal problem

$$\left(\rho_0 c^2 \Phi_z\right)_z + \rho_0 N^2 \Phi = 0, \quad \text{for } -h^- < z < h^+, \tag{4.4}$$

$$\Phi = 0, \quad \text{at } z = -h^- \text{ and } h^+, \tag{4.5}$$

where N is the buoyancy frequency defined as $N^2 = -(g/\rho_0)(\mathrm{d}\rho_0/\mathrm{d}z)$. In practice, to construct a two-layer fluid system based on a given realistic continuous stratification, the thicknesses $h^{\pm}$ and densities $\rho^{\pm}$ can be numerically determined by keeping the main parameters c, φ, ϑ given in (2.23), (2.32), (2.33) as close as those in the continuous medium (4.1)–(4.5), by virtue of the least squares method. This scheme is able to achieve the kinematic equivalence (approximately) between two-layered and continuous stratifications.

In the MITgcm simulation, the water depth is assumed to be 300 m. The continuous density distribution is shown in figure 1, calculated from the monthly averaged background temperature and salinity profiles (data from the World Ocean Atlas 2013). The kinematically equivalent layering yields $h^+ = 83$ m, $h^- = 217$ m and $R = \rho^+/\rho^- = 0.9983$, which are the parameters used in the following computations of the mBL equation and the KP equation. An important issue here is the preparation of the initial solitary wave in the MITgcm. As the solutions to the mBL equation (2.26*a*,*b*) and the KP equation (2.35) do not completely satisfy the primitive equations, an adjustment run is needed. We first insert the line soliton and the corresponding velocity field obtained from solving the mBL equation into the MITgcm and then run the model in the x–z plane. We let the program evolve until it reaches a steady state, taken as the initial solitary wave for the MITgcm. Despite quantitative differences, the result of the MITgcm model shows a similar circular refraction pattern as that in the mBL equation (figure 3*d* versus figure 3*b*), which confirms the validity of the mBL equation and indicates the failure of the KP equation in some cases. We note that a very recent study by Ryskamp *et al.* (2021) based on the KP equation shows a similar pattern (figure 5 in their paper) as our figure 3(*e*). Thus it is of great interest to revisit their problem based on an isotropic bi-directional model, for instance, the Benney–Luke equation.

In this paper, the modification to the classic Benney–Luke equation is the inclusion of topographic effects. The transverse variation of the topography modulates the wave pattern to some extent, as shown by the comparison between figure 3(*b*) and figure 3(*c*). As shown in figure 3(*f*), the interface fluctuations (denoted as η) at section lines $y = 0$ and 12.5 km imply that the existence of topography leads to an increase in wave amplitude and a decrease in wave speed. Nonetheless, the scales (2.15*a–f*) used in the derivation indicate that the height of topography is of the same order as the wave amplitude. Thus a significant topography should be used with precaution in numerical computations.

Next, we check the evolution of a partially bent solitary wave, composed of a truncated solitary wave of amplitude $\eta_0 = -30$ m as the middle stem, abruptly extended by two outgoing oblique solitary waves of amplitude $\eta_0 = -10$ m and bent angles $\pm 20^\circ$ (see figure 4*a*). Again, the result illustrates a significant disparity between the KP equation and the mBL equation (figure 4*b–c* versus figure 4*d–e*), which further manifests the feature of the isotropic model. The discontinuities at the conjunction regions eventually evolve into two circular diffraction patterns in the mBL equation rather than arched trailing waves in the KP equation. The transverse variation of the topography $b(y)$ modifies the waveform, increases its amplitude and slows the propagation speed, akin to figure 3.

https://doi.org/10.1017/jfm.2022.60 Published online by Cambridge University Press

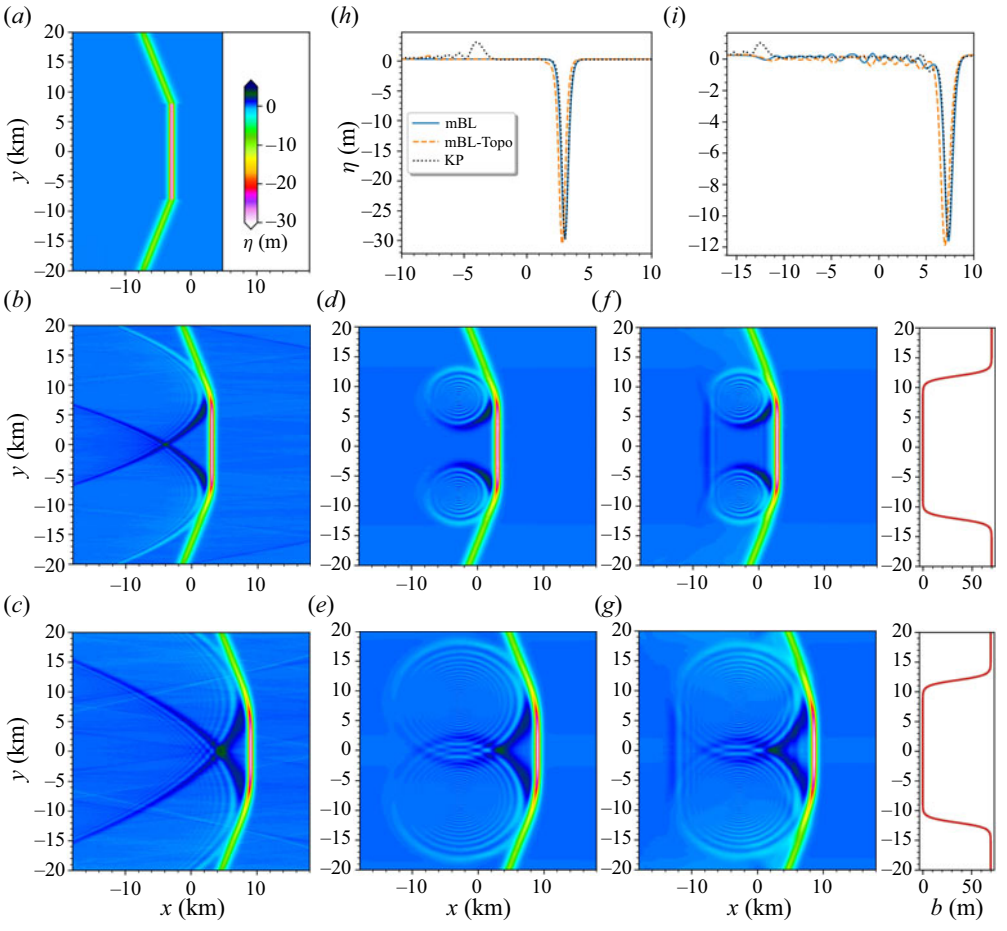

Figure 4. (*a*) Initial internal solitary waves with amplitudes $\eta_0 = -30$ m for the middle stem and $\eta_0 = -10$ m for oblique branches of bent angles $\pm 20^\circ$. (*b*,*c*) Snapshots of the wave pattern in the KP equation with a flat bottom at $t = 5400$ and 10 800 s, respectively. (*d*,*e*) Snapshots of the wave pattern in the mBL equation with a flat bottom at $t = 5400$ and 10 800 s, respectively. (*f*,*g*) Snapshots of the wave pattern at $t = 5400$ and 10 800 s, respectively, in the mBL equation in the presence of y-dependent topography $b(y)$ shown on the far right. (*h*,*i*) Interface fluctuations at $t = 10\,800$ s along section lines $y = 0$ and $y = 12.5$ km, respectively.

4.2. *X-shaped wave–wave interactions*

The oblique internal wave–wave interactions exhibit three-dimensional characteristics and likely give rise to peculiar wave patterns, as revealed by numerous observations in the ocean, primarily via satellite images (see, for example Hsu, Liu & Liu 2000; Xue *et al.* 2014). On this topic, the pioneering work of Miles (1977*a*,*b*) classifies the interaction as either 'strong' or 'weak' depending on the inclination angle between two solitons and theoretically describes 'Mach reflection' as the resonant interaction. In recent years, a series of progress was made by Chakravarty & Kodama (2008, 2009, 2013), who proposed a method to construct multi-soliton solutions to the KP equation. These solutions manifest themselves as an arbitrary number of line solitons in the far field and a novel wave pattern owing to the wave interaction in the near field. Based on their method, the interaction patterns observed in reality can be easily reproduced in theory (if applicable) via counting the number of solitons in the far field and measuring the amplitude and

https://doi.org/10.1017/jfm.2022.60 Published online by Cambridge University Press

slope of each soliton. Using their results and the variable-coefficient KP equation, Yuan *et al.* (2018*a*) investigated the topographic effects on the so-called V-shaped internal wave–wave interactions, which abound in oceans. In addition to the V-shaped interactions, the X-shaped internal wave–wave interactions (see the upper right corner of figure 2) are also very likely to occur in oceans, albeit few studies have specifically focussed on this type of interaction.

We first briefly introduce the work of Chakravarty & Kodama (2008, 2009, 2013). Note that the KP equation (2.31) can be transformed to the canonical form

$$(4\bar{\eta}_{\bar{t}} + 6\bar{\eta}\bar{\eta}_{\bar{x}} + \bar{\eta}_{\bar{x}\bar{x}\bar{x}})_{\bar{x}} + 3\bar{\eta}_{\bar{y}\bar{y}} = 0, \tag{4.6}$$

where new variables with overline are defined as

$$t = \left(\sqrt{\frac{27\vartheta}{2c^3}}\right)\bar{t}, \quad x - ct = \left(\sqrt{\frac{6\vartheta}{c}}\right)\bar{x}, \quad y = \left(\sqrt{\frac{6\vartheta}{c}}\right)\bar{y}, \quad \eta = \left(\frac{c}{\varphi}\right)\bar{\eta}. \tag{4.7a–d}$$

The soliton solution to (4.6) in the Wronskian form is represented by

$$\bar{\eta} = 2(\ln\tau)_{\bar{x}\bar{x}}, \tag{4.8}$$

where $\tau(\bar{x},\bar{y},\bar{t}) = Wr(f_1, f_2, \ldots, f_N)$, and Wr denotes the Wronskian of the functions f_n, which can be expressed as a sum of exponential functions, for $n = 1, 2, \ldots, N$,

$$f_n = \sum_{m=1}^{M} a_{nm}\exp(\Theta_m) \quad \text{with } \Theta_m = \sigma_m\bar{x} + \sigma_m^2\bar{y} - \sigma_m^3\bar{t}. \tag{4.9}$$

Obviously, the soliton solution depends on $M\,(>N)$ real parameters, ordered as $\sigma_1 < \sigma_2 < \cdots < \sigma_M$, and constants a_{nm} forming an $N \times M$ coefficient matrix $\mathbb{A}$ with $\mathrm{rank}(\mathbb{A}) = N$. Suppose we denote by $\chi(j_1, j_2, \ldots, j_N)$ the $N \times N$ minor of $\mathbb{A}$ obtained from columns $1 \leqslant j_1 < \cdots < j_N \leqslant M$, then to ensure a non-singular solution (4.8), all the $N \times N$ minors of $\mathbb{A}$ should be non-negative, i.e. $\chi(j_1, j_2, \ldots, j_N) \geqslant 0$. It was proved by Chakravarty & Kodama (2009) that as $\bar{y} \to \infty$, there exist N line solitons, while as $\bar{y} \to -\infty$, there are $M - N$ line solitons. For example, for $M = 2$ and $N = 1$, one line soliton exists as either $\bar{y} \to -\infty$ or $\bar{y} \to \infty$, and the $N \times M$ matrix $\mathbb{A} = (1, a)$, where $a > 0$ is a constant determining the location of the wave. Subsequently, $\tau(\bar{x},\bar{y},\bar{t})$ can be defined as

$$\tau = \exp(\Theta_1) + a\exp(\Theta_2), \tag{4.10}$$

and substituting (4.10) into the solution (4.8) yields

$$\bar{\eta} = \frac{\bar{k}^2}{2}\,\mathrm{sech}^2\left(\frac{\bar{k}\bar{x} + \bar{l}\bar{y} - \omega\bar{t} + \ln a}{2}\right), \tag{4.11}$$

where

$$\bar{k} = \sigma_2 - \sigma_1, \quad \bar{l} = \sigma_2^2 - \sigma_1^2, \quad \omega = \sigma_2^3 - \sigma_1^3 = \frac{\bar{k}^4 + 3\bar{l}^2}{4\bar{k}}. \tag{4.12a–c}$$

Equation (4.11) can be further rewritten in terms of physical variables as

$$\bar{\eta} = \bar{\eta}_0\,\mathrm{sech}^2\left[\bar{\Gamma}(\bar{x} + \bar{y}\tan\Psi - \bar{\varpi}\bar{t} + \bar{x}_0)\right], \tag{4.13}$$

where

$$\bar{\eta}_0 = \frac{\bar{k}^2}{2}, \quad \bar{\Gamma} = \sqrt{\frac{\bar{\eta}_0}{2}}, \quad \bar{\varpi} = \frac{1}{2}\bar{\eta}_0 + \frac{3}{4}\tan^2\Psi, \quad \bar{x}_0 = \frac{\ln a}{\sqrt{2\bar{\eta}_0}}, \tag{4.14a–d}$$

and Ψ is the inclination angle of the line soliton measured counterclockwise with respect to the y-axis. Upon noticing that the spatial scaling factors are the same, the angle Ψ is

https://doi.org/10.1017/jfm.2022.60 Published online by Cambridge University Press

unchanged under the transformation (4.7*a–d*), which can be expressed as

$$\tan\Psi = \frac{\bar{l}}{\bar{k}} = \sigma_1 + \sigma_2. \tag{4.15}$$

In practice, one can easily obtain $\bar{\eta}_0$ and Ψ from the field observation together with the transformation (4.7*a–d*), and then σ_1 and σ_2 can be recovered by solving $\bar{\eta}_0 = (\sigma_2 - \sigma_1)^2/2$ and (4.15). Eventually, a soliton solution to the KP equation is constructed.

The initial X-shaped wave can be prepared by intersecting two line solitons whose inclination angles with respect to the transverse y-direction are $\pm\Psi$ (see the right upper corner of figure 2). The amplitudes of two solitons, denoted by η_1 and η_2, do not necessarily have to be the same. Based on the aforementioned theory of the KP equation, the evolution of the initial X-shaped wave can be categorised into four types, corresponding to four different regions in the first quadrant of the $\eta_1 - \Psi$ plane (for a fixed η_2), as shown in figure 2. No analytic solutions were found to exist on the boundaries between different regions (i.e. the broken lines).

For case (a), we choose $\eta_1 = \eta_2 = -15$ m, which can be transformed to $\bar{\eta}_1 = \bar{\eta}_2 = 0.17$ based on the scaling (4.7*a–d*), and the boundary separating case (a) from other cases is depicted as $\sqrt{2\bar{\eta}_1} + \sqrt{2\bar{\eta}_2} = 2\tan\Psi_0$ that gives the critical angle $\Psi_0 \approx 30^\circ$. Here we choose $\Psi = 33^\circ > \Psi_0$. Snapshots of the wave pattern at different times are shown in figure 5, where the most remarkable features are the phase shift in the interaction zone (see a zoom-in in figure 6) and the trailing waves arising from the self-adjustment process. When the results are scrutinised, the discrepancy in wave amplitude between the KP equation and the mBL equation is conspicuous, and the latter is rendered with a slightly smaller amplitude (see figure 5*h–i* or figure 6*d*). It is shown in figure 5(*h*) that the variation of bottom topography in the direction of internal wave propagation augments the wave amplitude in the interaction zone, and no obviously disparate trailing waves are generated.

In solution (4.8), two branches of the initial X-shaped wave are described by two sets of parameters for case (a), $(\sigma_1, \sigma_2) = (-0.61, -0.04)$ and $(\sigma_3, \sigma_4) = (0.04, 0.61)$. Because $\bar{\eta}_1 = \bar{\eta}_2$, the phase shifts (denoted by $\delta\bar{x}$ in the transformed plane (4.7*a–d*)) for the upper and lower branches turn out to be the same, which can be predicted by

$$\delta\bar{x} = \frac{\Theta_{12}}{\sigma_2 - \sigma_1}, \quad \Theta_{12} = -\ln\Delta_0, \quad 0 < \Delta_0 = \frac{(\sigma_3 - \sigma_2)(\sigma_4 - \sigma_1)}{(\sigma_4 - \sigma_2)(\sigma_3 - \sigma_1)} < 1, \tag{4.16a–c}$$

leading to $\delta x = 366$ m in the original variables. However, the numerical results are $\delta x = 326$ m for the KP equation, $\delta x = 413$ m for the mBL equation and $\delta x = 439$ m for the mBL equation with the topography $b(x)$ (see figure 6), and plausibly all of them can be considered as good approximations. Note that the phase shift is independent of time. Similarly, this theoretical result also predicts the wave amplitude in the interaction zone, namely

$$\bar{\eta}_{max} = \bar{\eta}_1 + \bar{\eta}_2 + 2\frac{1 - \sqrt{\Delta_0}}{1 + \sqrt{\Delta_0}}\sqrt{\bar{\eta}_1\bar{\eta}_2}, \tag{4.17}$$

which gives $\eta_{max} = -41$ m after being converted to the original variables. It is shown in figure 6(*d*) that the numerical result of the KP equation asymptotically approaches the theoretical prediction. However, the numerical solution to the mBL equation is still a bit off the theoretical value after 6 h of evolution.

Next, we investigate case (b) by illuminating a quantitative example of the schematic in figure 2(*b*). Here we choose the amplitudes $\eta_1 = \eta_2 = -15$ m and inclination angle $\Psi = 25^\circ$. As time evolves, a separation commences from the interaction zone resulting

https://doi.org/10.1017/jfm.2022.60 Published online by Cambridge University Press

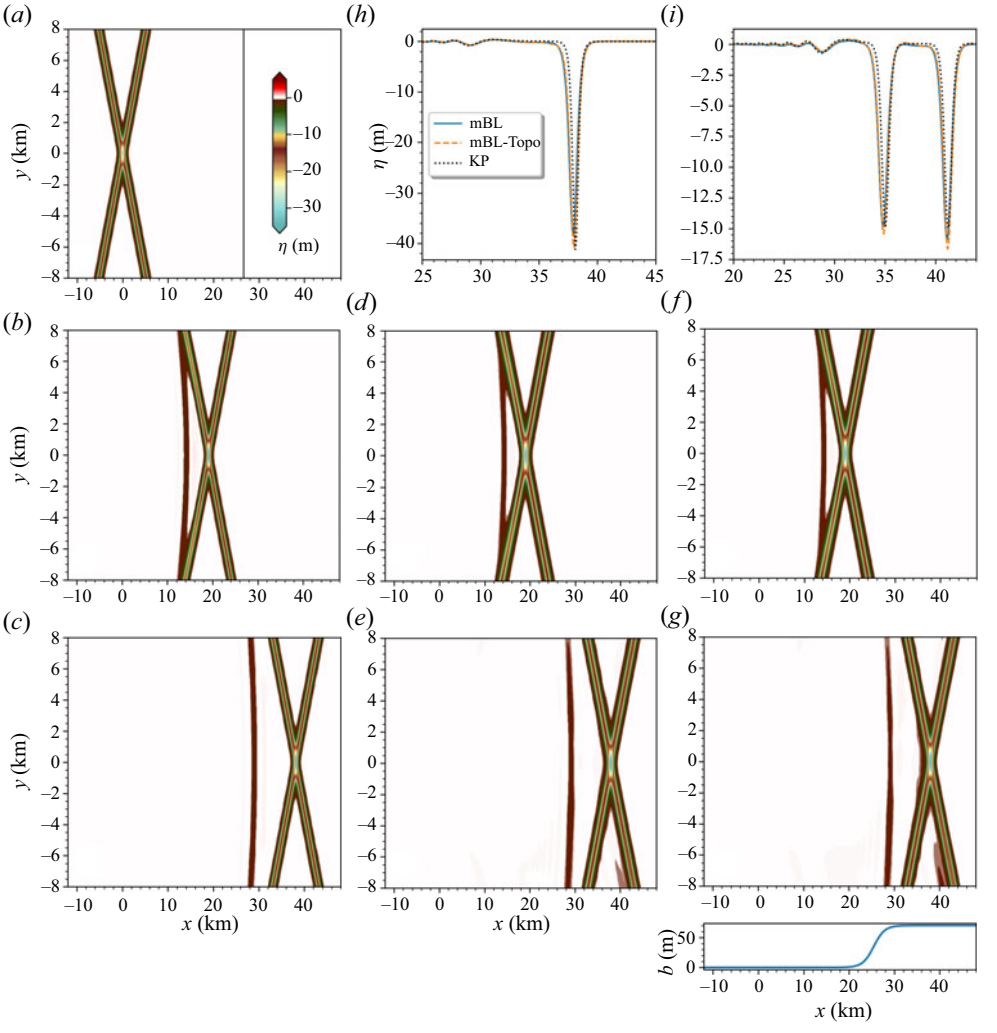

Figure 5. (*a*) Initial X-shaped wave with amplitudes $\eta_1 = \eta_2 = -15$ m and inclination angle $\Psi = 33^\circ$. (*b*,*c*) Snapshots of the wave pattern in the KP equation with a flat bottom at $t = 1.5 \times 10^4$ and 3.0×10^4 s, respectively. (*d*,*e*) Snapshots of the wave pattern in the mBL equation with a flat bottom at $t = 1.5 \times 10^4$ and 3.0×10^4 s, respectively. (*f*,*g*) Snapshots of the wave patterns at $t = 1.5 \times 10^4$ and 3.0×10^4 s, respectively, in the mBL equation with x-dependent topography $b(x)$ shown on the extreme right. (*h*,*i*) Interface fluctuations at $t = 3.0 \times 10^4$ s along section lines $y = 0$ and $y = 5$ km, respectively. For the results of the mBL equation with topography, the actual computational domain in the x-direction is twice that shown in the figure to allow for periodicity.

in an opening isosceles trapezium (figures 7 and 8). Note that the equivalence of the leg lengths arises from the initial setting $\eta_1 = \eta_2$. Considering numerical errors, we do not detect perceptible differences in waveform between the KP equation and the mBL equation, though there is a slight discrepancy in wave amplitude. As in case (a), it is clear that the shoaling can augment the wave amplitude; see the comparisons in figure 7(*h*–*i*).

In the framework of the KP equation, the theoretical descriptions of case (b) are much more complicated than those of case (a), whose behaviours within the interaction zone depend only on several parameters determined by the initial waves. It is not difficult to

https://doi.org/10.1017/jfm.2022.60 Published online by Cambridge University Press

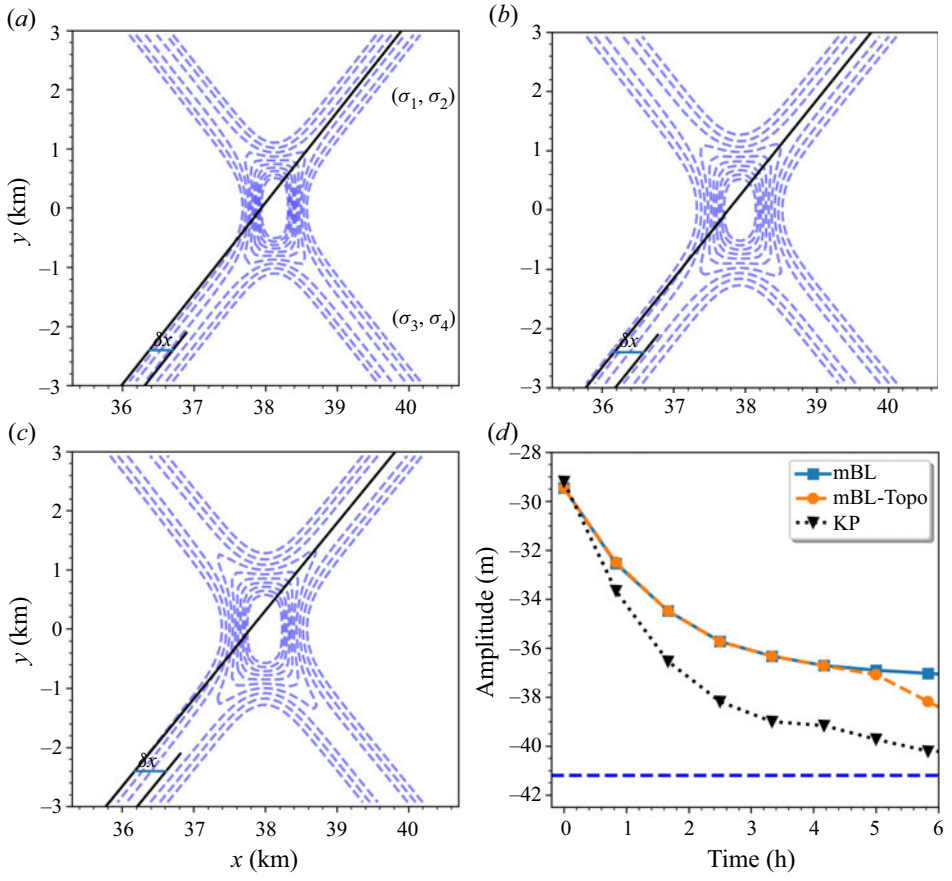

Figure 6. (*a–c*) Close-ups of the interaction zone of figure 5 at $t = 3.0 \times 10^4$ s. The phase shifts (denoted by δx) for the KP equation, the mBL equation and the mBL equation with topography $b(x)$ are respectively highlighted. (*d*) Time series of the wave amplitude at the intersection point computed with different models, together with the asymptotic prediction (blue dashed line).

see that $N = 2$ and $M = 4$ for case (b), and therefore the coefficient matrix $\mathbb{A}$ can be represented as

$$\mathbb{A} = \begin{pmatrix} 1 & 0 & -a & -b \\ 0 & 1 & c & d \end{pmatrix}, \tag{4.18}$$

where $a, b, c, d > 0$ are free parameters determining the locations of solitons, their phase shifts and the onset of the trapezium pattern. The minors of $\mathbb{A}$ satisfy $\chi(j_1, j_2) \geqslant 0$ to ensure the existence of non-singular solutions and particularly, $bc - ad > 0$. In this situation, the initial two branches can be delineated by the pairs (σ_1, σ_3) and (σ_2, σ_4), as illustrated in figure 8(*a*). These parameters can be easily calculated from the amplitudes and inclination angles of the given initial data. Actually, using (4.11) and (4.15), one obtains $(\sigma_1, \sigma_2, \sigma_3, \sigma_4) = (-0.52, -0.06, 0.06, 0.52)$ for this example. The phase shift of the upper right branch ($\bar{x} > 0$ and $\bar{y} \gg 0$) is represented by

$$\Theta_{13}^{+} = \ln \frac{\sigma_4 - \sigma_1}{\sigma_4 - \sigma_3} - \ln \frac{F}{b}, \tag{4.19}$$

https://doi.org/10.1017/jfm.2022.60 Published online by Cambridge University Press

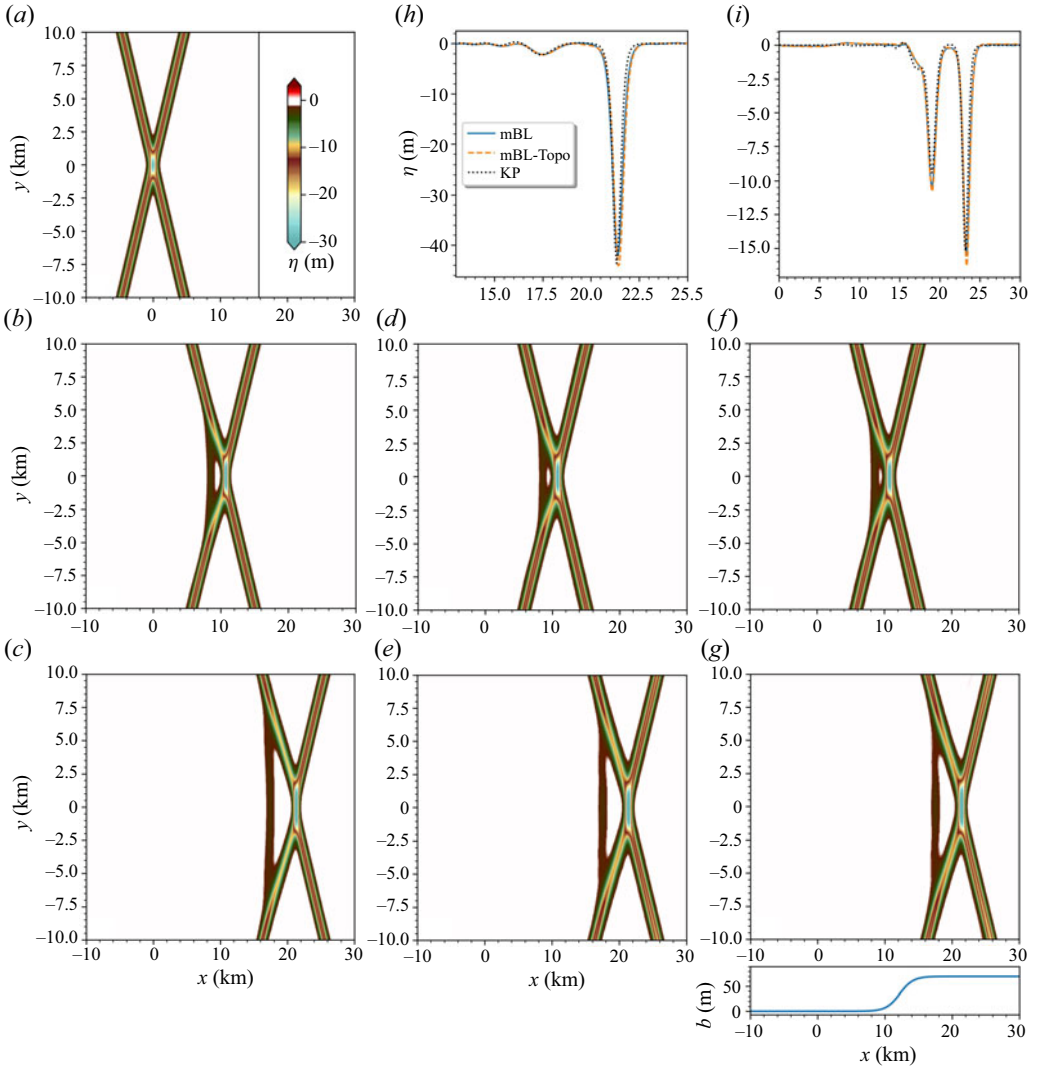

Figure 7. (*a*) Initial X-shaped pattern with amplitudes $\eta_1 = \eta_2 = -15$ m and inclination angle $\Psi = 25^\circ$. (*b*,*c*) Snapshots of the wave pattern in the KP equation with a flat bottom at $t = 9 \times 10^3$ and 1.8×10^4 s, respectively. (*d*,*e*) Snapshots of the wave pattern in the mBL equation with a flat bottom at $t = 9 \times 10^3$ and 1.8×10^4 s, respectively. (*f*,*g*) Snapshots of the wave pattern at $t = 9 \times 10^3$ and 1.8×10^4 s, respectively, in the mBL equation with x-dependent topography $b(x)$ shown under panel (*g*). (*h*,*i*) Interface fluctuations at $t = 1.8 \times 10^4$ s along section lines $y = 0$ and $y = 5$ km, respectively. For the results of the mBL equation with topography, the actual computational domain in the x-direction is twice that shown in the figure to allow for periodicity.

where $F = \chi(3, 4) = bc - ad$, while for the lower left branch ($\bar{x} < 0$ and $\bar{y} \ll 0$),

$$\Theta_{13}^{-} = \ln \frac{\sigma_2 - \sigma_1}{\sigma_3 - \sigma_2} - \ln c. \tag{4.20}$$

https://doi.org/10.1017/jfm.2022.60 Published online by Cambridge University Press

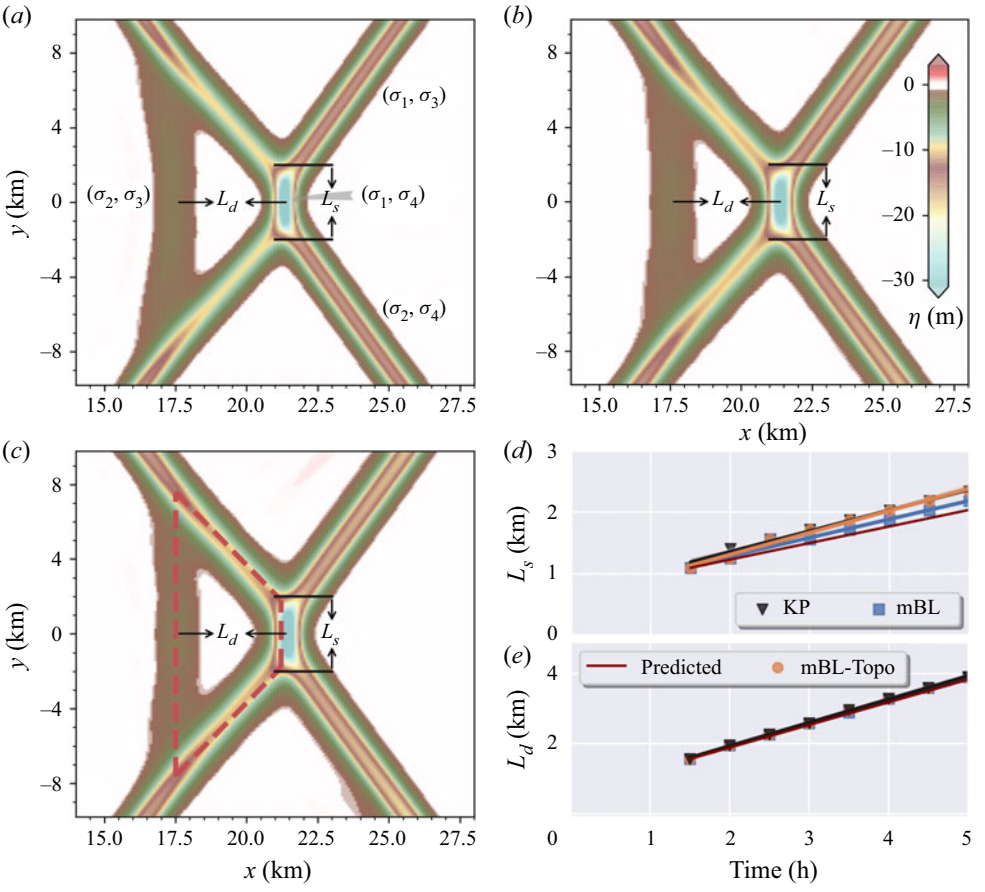

Figure 8. (*a–c*) Close-ups of the interaction zone of figure 7 at $t = 1.8 \times 10^4$ s. The lengths of the middle stem L_s and the widths of the generated 'trapezium' L_d are highlighted for the KP equation, the mBL equation and the mBL equation with topography $b(x)$. (*d,e*) Time series of L_s and L_d computed with different models along with the theoretically predicted values.

Similarly, the phase shifts for the upper left branch ($\bar{x} < 0$ and $\bar{y} \gg 0$) and lower right branch ($\bar{x} > 0$ and $\bar{y} \ll 0$) read

$$\Theta_{24}^{+} = \ln\frac{\sigma_3 - \sigma_2}{\sigma_4 - \sigma_3} - \ln\frac{F}{c}, \quad \Theta_{24}^{-} = \ln\frac{\sigma_2 - \sigma_1}{\sigma_4 - \sigma_1} - \ln b, \tag{4.21a,b}$$

respectively. Thus, in theory, the phase shifts of the two branches are $\Theta_{13} = \Theta_{13}^{+} - \Theta_{13}^{-}$ and $\Theta_{24} = \Theta_{24}^{+} - \Theta_{24}^{-}$, which depend not only on σ_j but also on the free parameters a, b, c, d. Nonetheless, the phase shift along the $\bar{y}$-direction is conserved because

$$\Theta_{13}^{+} + \Theta_{24}^{-} = \Theta_{24}^{+} + \Theta_{13}^{-} = \ln\frac{\sigma_2 - \sigma_1}{\sigma_4 - \sigma_3} - \ln F. \tag{4.22}$$

In contrast to the phase shift depending on free parameters, we can determine the length of the stem $\bar{L}_s$, the asymptotic amplitude of the stem $\bar{\eta}_{\max}$ and the width of the opening trapezium $\bar{L}_d$, using the properties of initial waves (see figure 8). Here the upper right branch is described by (σ_1, σ_3) and the stem by (σ_1, σ_4). Therefore, the ridges of these

https://doi.org/10.1017/jfm.2022.60 Published online by Cambridge University Press

two parts are given by $\Theta_1 = \Theta_3$ and $\Theta_1 = \Theta_4$, respectively. Recalling the definition of Θ_j given in (4.9), one obtains

$$\bar{x} + (\sigma_3 + \sigma_1)\bar{y} = \left(\sigma_1^2 + \sigma_1\sigma_3 + \sigma_3^2\right)\bar{t}, \tag{4.23}$$

$$\bar{x} = \left(\sigma_1^2 + \sigma_1\sigma_4 + \sigma_4^2\right)\bar{t}, \tag{4.24}$$

upon noting that $\sigma_1 + \sigma_4 = 0$ and $\sigma_2 + \sigma_3 = 0$. The wave pattern is symmetric about the x-axis given $\eta_1 = \eta_2$, and thus the length of the stem $\bar{L}_s = 2\bar{y}$, where $\bar{y}$ indicates the location of the intersection point. A simple manipulation of (4.23)–(4.24) yields

$$\bar{L}_s = 2\sigma_3\bar{t}. \tag{4.25}$$

In the long-time evolution, the amplitude of the stem approaches the asymptotic value given by

$$\bar{\eta}_{max} = \tfrac{1}{2}(\sigma_4 - \sigma_1)^2. \tag{4.26}$$

The width of the opening trapezium, $\bar{L}_d$, depends on the phase speed discrepancy between the stem and the other parallel side delineated by (σ_2, σ_3), which takes the form

$$\bar{L}_d = \left(\sigma_4^2 - \sigma_3^2\right)\bar{t}. \tag{4.27}$$

It is clear that both the predicted $\bar{L}_s$ and $\bar{L}_d$ are linear functions of time, and comparisons between the theoretical predictions and numerical simulations of different models are illustrated in figure 8(*d–e*). These comparisons are generally in good agreement, although slight differences, partly attributed to insufficient evolution time, are inevitable. This is shown, for example, by the gap between the amplitude of the stem $\eta \approx -44$ m (figure 7*h*) at the termination time of the computation $t = 1.8 \times 10^4$ s and the predicted asymptotic value $\eta_{max} = -49$ m.

From the physical point of view, case (c) and case (d) are of the same dynamical and kinematical properties by a simple reversal of the y-axis; thus, we confine ourselves to case (c). Here we choose wave amplitudes $\eta_1 = -5$ m (denoted by (σ_2, σ_3)) and $\eta_2 = -15$ m (denoted by (σ_1, σ_4)), together with the inclination angle $\Psi = 5^\circ$ which is smaller than the critical angle $\Psi_0 = \text{atan}(\sqrt{\bar{\eta}_2/2} - \sqrt{\bar{\eta}_1/2}) \approx 7^\circ$. It is calculated that $(\sigma_1, \sigma_2, \sigma_3, \sigma_4) = (-0.25, -0.21, 0.12, 0.33)$ based on the transformation (4.7*a–d*). By letting $\Theta_1 = \Theta_4$ and $\Theta_2 = \Theta_3$, one obtains

$$\left.\begin{aligned} \bar{x} + (\sigma_1 + \sigma_4)\bar{y} &= (\sigma_1^2 + \sigma_1\sigma_4 + \sigma_4^2)\bar{t}, \\ \bar{x} + (\sigma_2 + \sigma_3)\bar{y} &= (\sigma_2^2 + \sigma_2\sigma_3 + \sigma_3^2)\bar{t}, \end{aligned}\right\} \tag{4.28}$$

and thus the location of the intersection point can be expressed as

$$\bar{L}_x = \frac{7(\sigma_1 + \sigma_4)^2 + (\sigma_3 - \sigma_2)^2 - 8\sigma_1\sigma_4}{8}\,\bar{t} = \frac{\bar{\eta}_1 + \bar{\eta}_2 + 3\tan^2\Psi}{4}\,\bar{t}, \tag{4.29}$$

$$\bar{L}_y = \frac{(\sigma_1^2 + \sigma_1\sigma_4 + \sigma_4^2) - (\sigma_2^2 + \sigma_2\sigma_3 + \sigma_3^2)}{(\sigma_1 + \sigma_4) - (\sigma_2 + \sigma_3)}\,\bar{t} = \frac{\bar{\eta}_2 - \bar{\eta}_1}{4\tan\Psi}\,\bar{t}. \tag{4.30}$$

The intersection point moves in the positive y-direction owing to $\eta_2 > \eta_1$ (see figure 9). The numerical results of L_y for model equations are illustrated in figure 10, which show

https://doi.org/10.1017/jfm.2022.60 Published online by Cambridge University Press

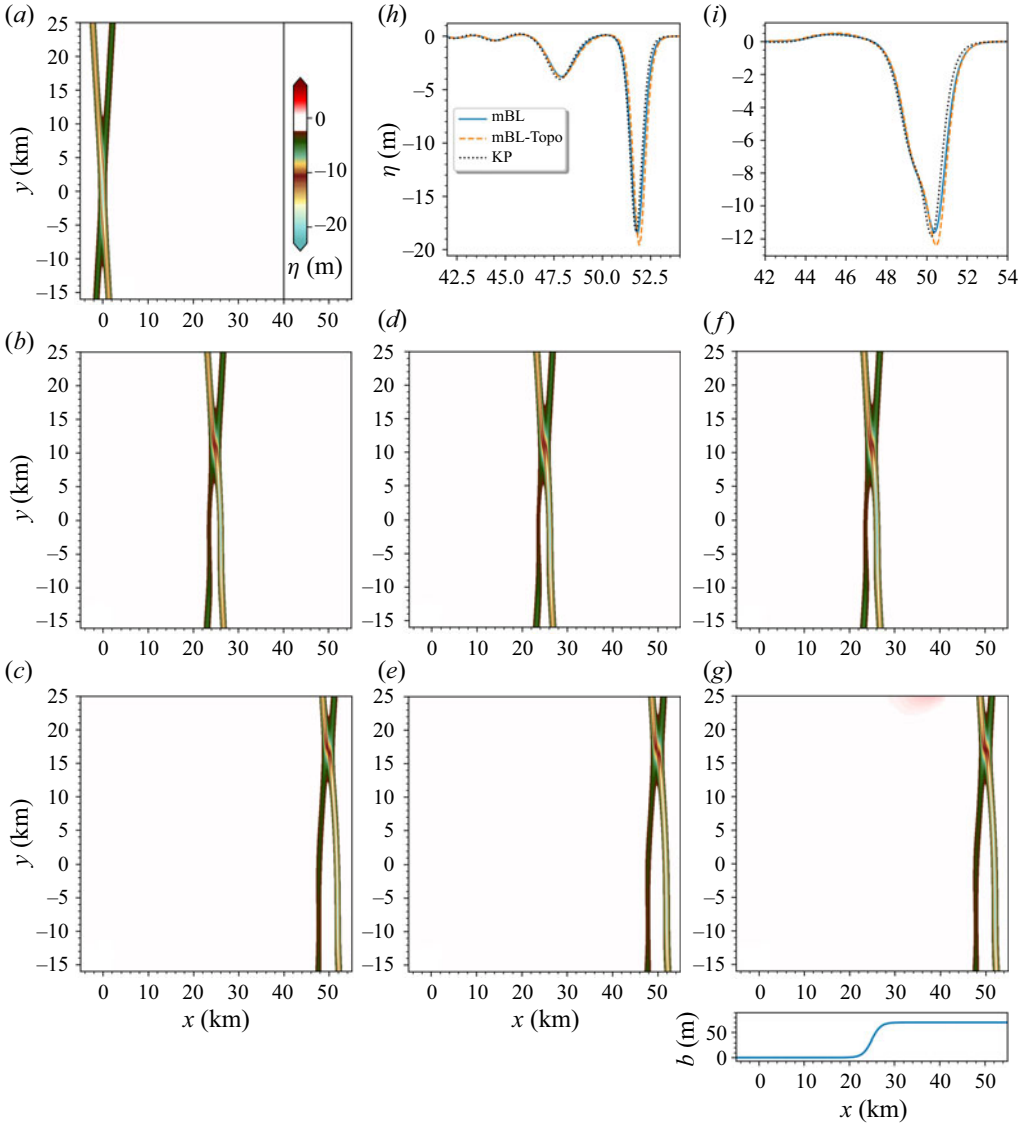

Figure 9. (*a*) Initial X-shaped pattern with amplitudes $\eta_1 = -5$ m, $\eta_2 = -15$ m and inclination angle $\Psi = 5^\circ$. (*b*,*c*) Snapshots of the wave pattern in the KP equation with a flat bottom at $t = 2.4 \times 10^4$ and 4.8×10^4 s, respectively. (*d*,*e*) Snapshots of the wave pattern in the mBL equation with a flat bottom at $t = 2.4 \times 10^4$ and 4.8×10^4 s, respectively. (*f*,*g*) Snapshots of the wave pattern at $t = 2.4 \times 10^4$ and 4.8×10^4 s, respectively, in the mBL equation with x-dependent topography $b(x)$ shown under panel (*g*). (*h*,*i*) Interface fluctuations at $t = 4.8 \times 10^4$ s along section lines $y = 0$ and $y = 16$ km, respectively. For the results of the mBL equation with topography $b(x)$, the actual computational domain in the x-direction is twice that shown in the figure to allow for periodicity.

good agreement with the theoretical prediction. The phase shifts for the two branches are

$$\overline{\delta x}_{ij} = -\frac{1 + \ln \Delta_0}{\sigma_j - \sigma_i}, \quad \Delta_0 = \frac{(\sigma_4 - \sigma_2)(\sigma_3 - \sigma_1)}{(\sigma_4 - \sigma_3)(\sigma_2 - \sigma_1)}, \tag{4.31a,b}$$

https://doi.org/10.1017/jfm.2022.60 Published online by Cambridge University Press

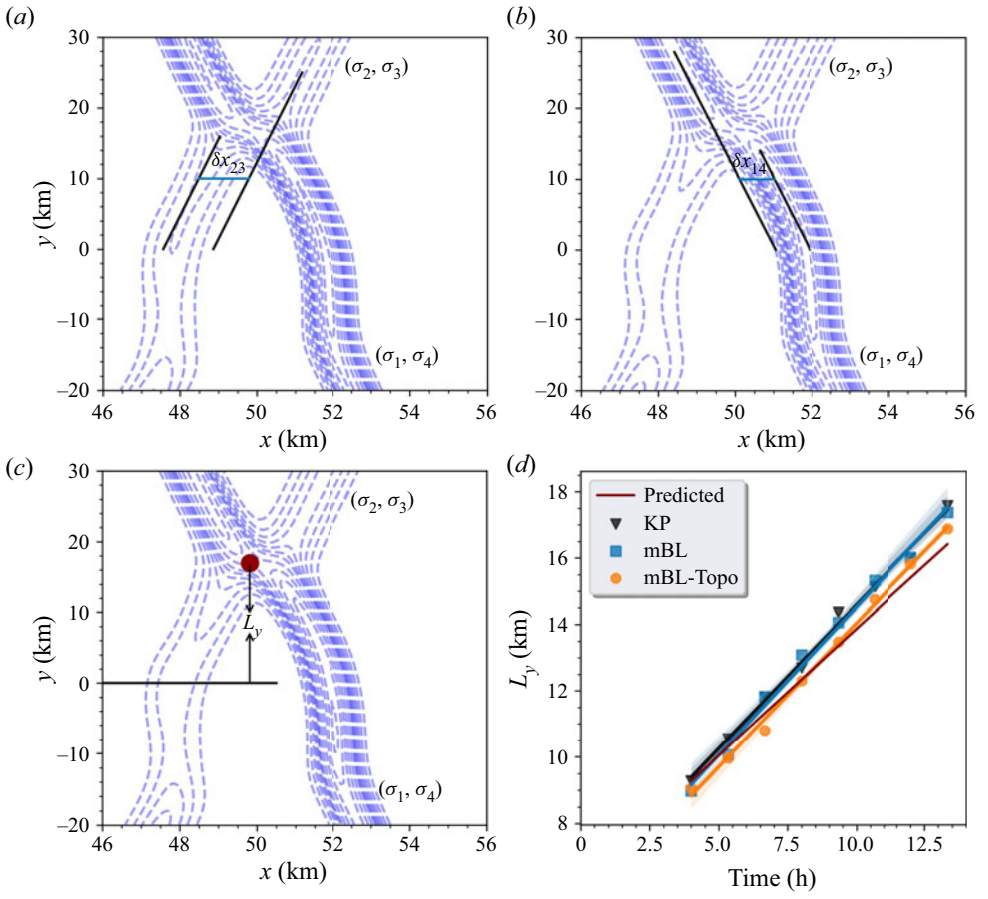

Figure 10. (*a–c*) Close-ups of the interaction zone of figure 9 at time $t = 4.8 \times 10^4$ s. The phase shifts δx_{14} and δx_{23} of the two branches and the location of the intersection point in the y-direction L_y are highlighted for the KP equation, the mBL equation and the mBL equation with topography $b(x)$, respectively. (*d*) Time series of L_y computed with different models together with the theoretically predicted values.

where the subscript (i, j) is either $(1, 4)$ or $(2, 3)$, representing the branches of the initial X-shaped wave. As shown in figure 10, the phase shifts of the branch characterised by (σ_1, σ_4) are $\delta x_{14} = 1.1$ km, 0.9 km and 1.0 km for the KP equation, the mBL equation and the mBL equation with topography, respectively, in comparison with $\delta x_{14} = 1.0$ km predicted by (4.31*a*,*b*). Similarly, the numerical results $\delta x_{23} = 1.3$ km, 1.4 km, 1.4 km for the three models are close to the theoretical prediction $\delta x_{23} = 1.7$ km for the branch (σ_2, σ_3).

4.3. *Truncated X-shaped wave–wave interactions*

Because the cases mentioned above focus on the central parts of wave interaction zones, which are of great interest for some scenarios, we apply a windowing method in computations. As a consequence, the propagation of waves in the y-direction is limited. Nevertheless, the realistic ocean should be considered open for internal waves, although the along-crest width can be several hundred kilometres long. Thus, it is informative to

https://doi.org/10.1017/jfm.2022.60 Published online by Cambridge University Press

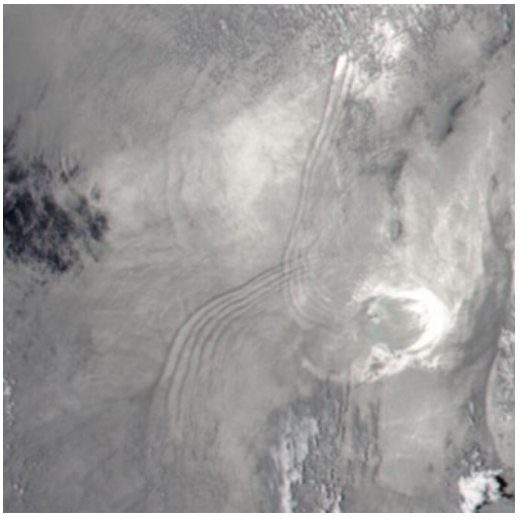

Figure 11. An NOAA-20 VIIRS satellite image taken on 16 May 2020, with the left-bottom corner located at 20.1228°N, 115.6389°E and the right-top at 21.61°N, 117.133°E.

investigate the cases in which waves can propagate freely in all horizontal directions. To illustrate this circumstance, we show in figure 11 a radar image photographed in the South China Sea. The subsequent computations display evolutions of initial X-shaped internal waves in an open sea.

The set-ups are the same as those in the previous three cases except that an envelope locally confined in the y-direction is imposed on the initial X-shaped waves. Figures 12–15 demonstrate the time evolutions of these truncated patterns. We note an important consequence immediately that the coherent wave–wave interaction patterns (see figures 5–10) are disrupted owing to dispersive effects. After the initial launch, two front edges of the truncated wave begin to collapse and spread in the y-direction at the cost of decreasing the wave amplitude from the periphery to centre gradually. Meanwhile, the y-components of the propagation velocities of the two initial waves are opposite. As a result, the intersection zone moves towards the front edges of the pattern, which finally manifests as a leading wave connected by two arched trailing branches. Another significant feature is the post-interaction waves, especially the trailing waves of opposite polarity (waves of positive displacement with red colour in figures 12–15), whose emergence can be explained by mass conservation (Yuan *et al.* 2018*b*).

As waves can propagate freely in all horizontal directions, the discrepancies between the KP and mBL equations are evident. One of the most striking differences is the opening degree of trailing waves. It can be seen from panels (*b*–*g*) of figures 12, 13 and 15 that waves branch at wider angles in the KP equation, attributing to its anisotropic nature. Moreover, wave amplitudes given by the two equations are significantly different, even a difference of double, as shown in figure 13(*h*). To put the validity of the mBL equation on a firmer footing, again, we conduct a comparison with the MITgcm model, as illustrated in figure 14, which verifies the use of the mBL equation as a better approximation to the full Euler equations for some cases of practical relevance. These results showcase, to a considerable extent, the advantage of the isotropic property of the mBL equation. Note that the topographic effects play a

https://doi.org/10.1017/jfm.2022.60 Published online by Cambridge University Press

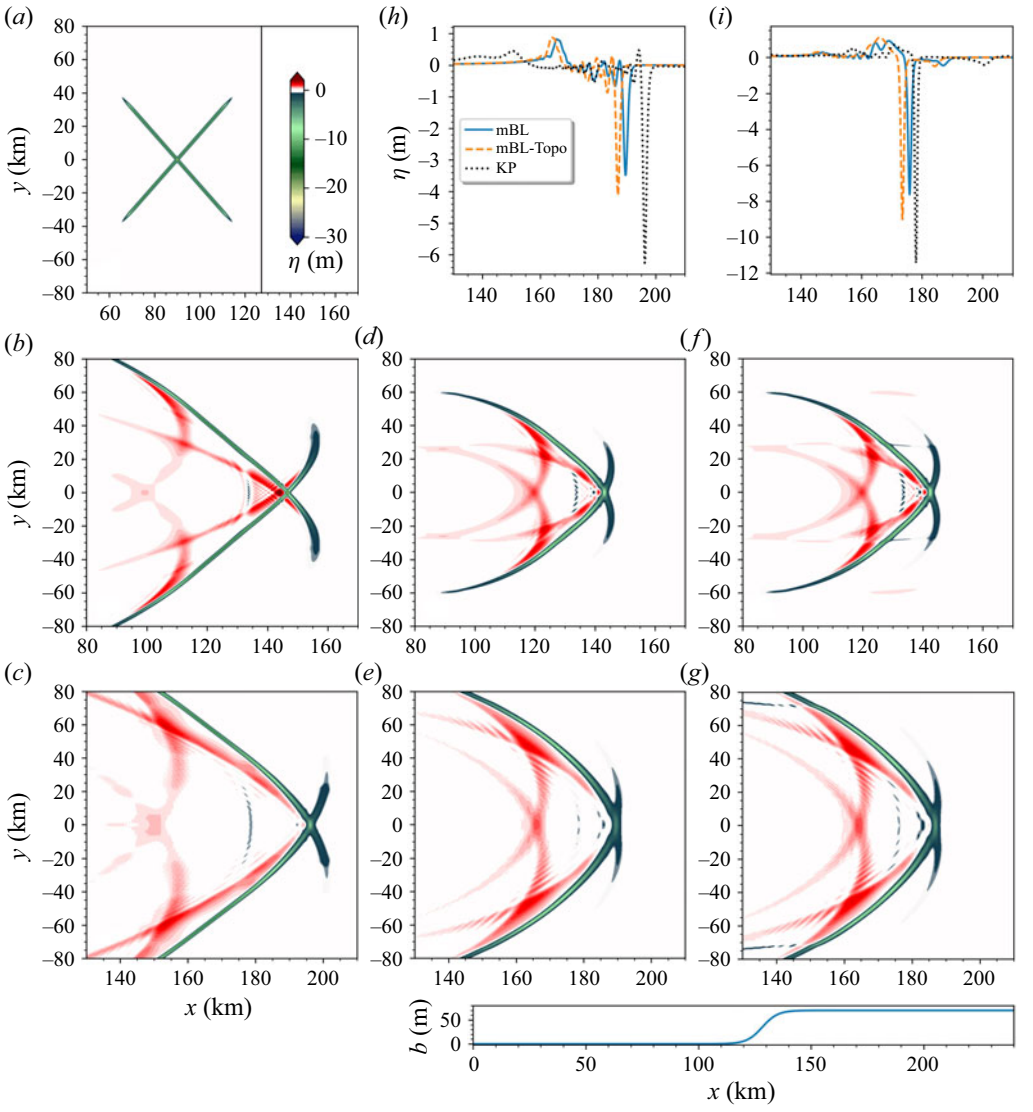

Figure 12. (*a*) Initial truncated X-shaped pattern with amplitudes $\eta_1 = \eta_2 = -15$ m and inclination angle $\Psi = 33°$; same as those in figure 5. (*b*,*c*) Snapshots of the wave pattern in the KP equation with a flat bottom at $t = 4.5 \times 10^4$ and 9.0×10^4 s, respectively. (*d*,*e*) Snapshots of the wave pattern in the mBL equation with a flat bottom at $t = 4.5 \times 10^4$ and 9.0×10^4 s, respectively. (*f*,*g*) Snapshots of the wave pattern at $t = 4.5 \times 10^4$ and 9.0×10^4 s, respectively, in the mBL equation with x-dependent topography $b(x)$ shown under panel (*g*). (*h*,*i*) Interface fluctuations at $t = 9.0 \times 10^4$ s along section lines $y = 0$ and $y = 40$ km, respectively. For the results of the mBL equation with topography $b(x)$, the actual computational domain in the x-direction is twice that shown in the figure to allow for periodicity.

more significant role in modulating the characteristics of wave evolution, not only the waveform but also the wave amplitude and propagation speed (see panels (*h*) and (*i*) of figures 12, 13, 15), compared with the previous three cases. To further examine the effect of bottom gradients, we illustrate two typical cases in figure 16 where truncated X-shaped waves propagate over the shoaling topography superposed by submarine canyon

https://doi.org/10.1017/jfm.2022.60 Published online by Cambridge University Press

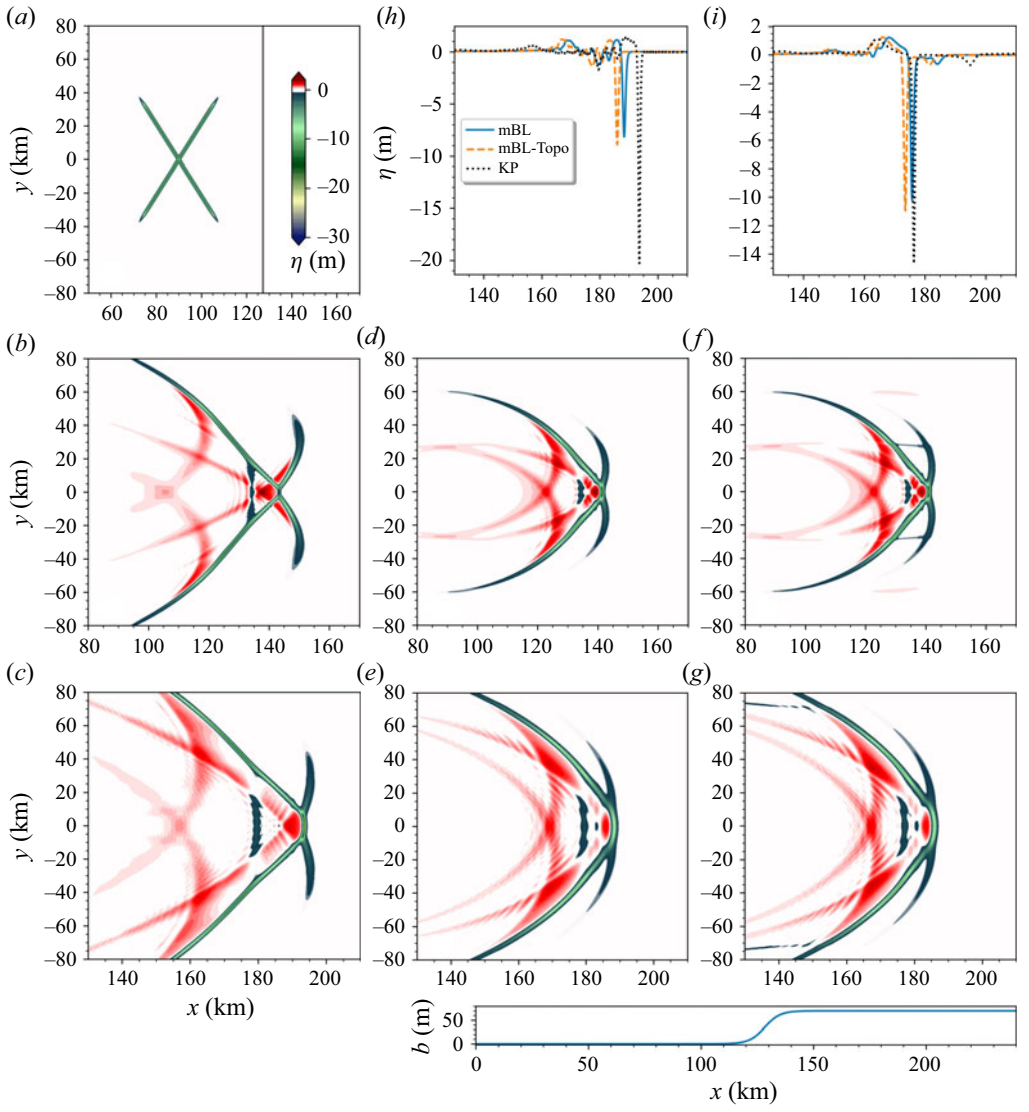

Figure 13. (*a*) Initial truncated X-shaped pattern with amplitudes $\eta_1 = \eta_2 = -15$ m and inclination angle $\Psi = 25^\circ$; same as those in figure 7. (*b*,*c*) Snapshots of the wave pattern in the KP equation with a flat bottom at $t = 4.5 \times 10^4$ and 9.0×10^4 s, respectively. (*d*,*e*) Snapshots of the wave pattern in the mBL equation with a flat bottom at $t = 4.5 \times 10^4$ and 9.0×10^4 s, respectively. (*f*,*g*) Snapshots of the wave pattern at $t = 4.5 \times 10^4$ and 9.0×10^4 s, respectively, in the mBL equation with x-dependent topography $b(x)$ shown under panel (*g*). (*h*,*i*) Interface fluctuations at $t = 9.0 \times 10^4$ s along section lines $y = 0$ and $y = 40$ km, respectively. For the results of the mBL equation with topography $b(x)$, the actual computational domain in the x-direction is twice that shown in the figure to allow for periodicity.

and plateau. Examples are motivated by the realistic ocean topography, such as the Hudson Canyon. It is clear that the canyon (plateau) slightly accelerates (slows) the wave propagation on the shoaling topography, engendering a distortion along the crest where small-amplitude waves emanate from, thereby reshaping wave patterns and altering wave amplitudes.

https://doi.org/10.1017/jfm.2022.60 Published online by Cambridge University Press

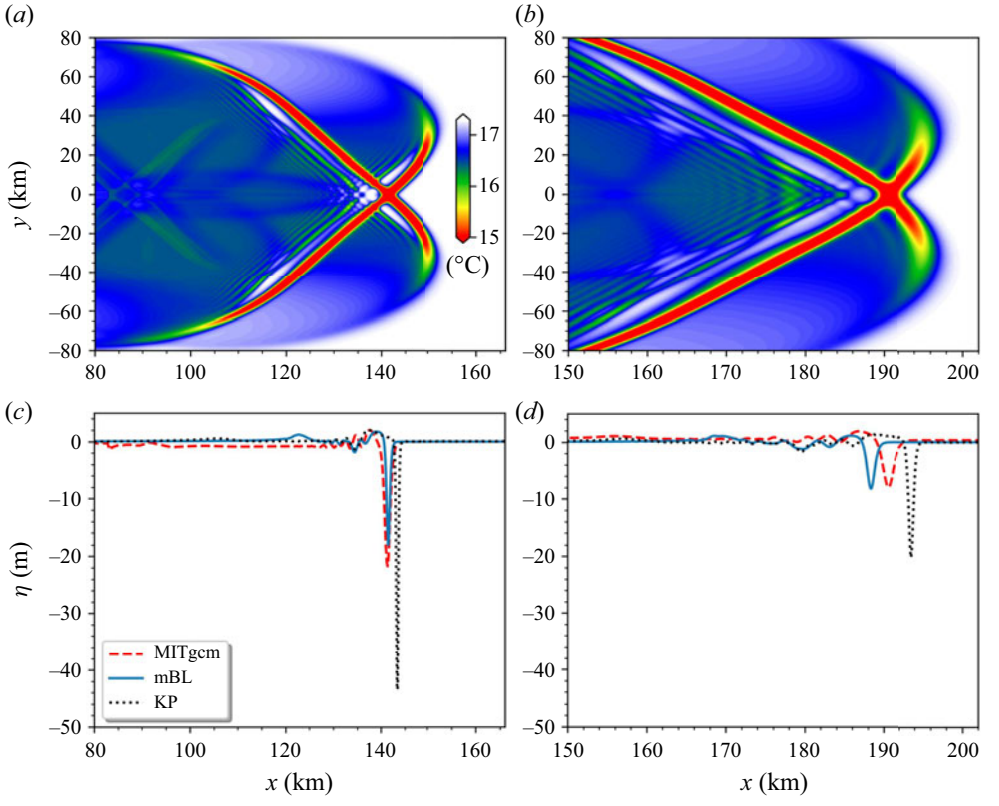

Figure 14. (*a*,*b*) Horizontal views of the temperature profile in the MITgcm simulation at $t = 4.5 \times 10^4$s and $t = 9.0 \times 10^4$ s, respectively. Note that the initial waves are the same as those in figure 13(*a*). (*c*,*d*) Comparisons of the interface fluctuation at $t = 4.5 \times 10^4$ s and $t = 9.0 \times 10^4$ s, respectively, along the section line $y = 0$.

5. Concluding remarks

In this paper, the mBL equation has been derived for internal waves in a two-fluid system with the rigid-lid approximation and variable bottom topography. The model features the isotropic and bi-directional nature and can be numerically implemented to study oblique internal wave–wave interactions, as well as the topographic effects on wave propagation. It is well known that the KP equation is the most widely used model in the context of horizontally two-dimensional internal waves, and indeed, it has a large range of validity inherited from its parent, the KdV equation. Nonetheless, we argue that in some general scenarios, the mBL equation presents more accurate results than the KP equation, which is attributed to the characteristics of isotropy and bi-directional propagation held by the former model. These characters can be easily understood from the linear dispersion relation. For a monochromatic wave with the wavenumber $\boldsymbol{k} = (k_x, k_y)$ and frequency ω, in the absence of bottom topography, the dispersion relations for the KP equation (2.31) and the mBL equation (2.24) read

$$\omega = -\vartheta k_x^3 + ck_x + \frac{c}{2}\frac{k_y^2}{k_x}, \quad \omega^2 = \frac{c^2|\boldsymbol{k}|^2}{1+\alpha|\boldsymbol{k}|^2}, \tag{5.1a,b}$$

respectively. It is clear that for the mBL equation, the wave frequency depends entirely on the modulus of the wavenumber vector, and the dispersion relation is hence isotropic, in

https://doi.org/10.1017/jfm.2022.60 Published online by Cambridge University Press

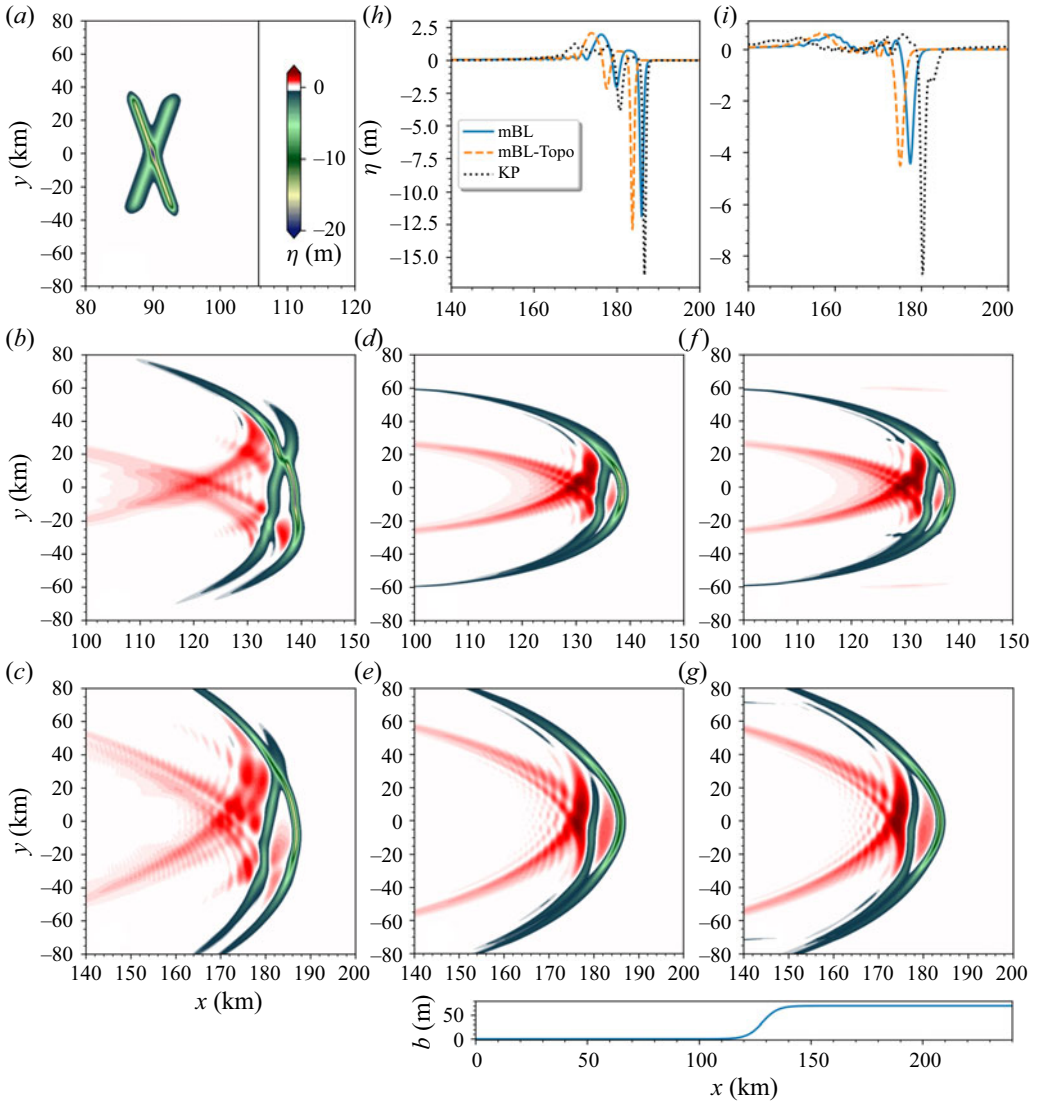

Figure 15. (*a*) Initial truncated X-shaped pattern with amplitudes $\eta_1 = -5$ m, $\eta_2 = -15$ m and inclination angle $\Psi = 5^\circ$; same as those in figure 9. (*b*,*c*) Snapshots of the wave pattern in the KP equation with a flat bottom at $t = 4.5 \times 10^4$ and 9.0×10^4 s, respectively. (*d*,*e*) Snapshots of the wave pattern in the mBL equation with a flat bottom at $t = 4.5 \times 10^4$ and 9.0×10^4 s, respectively. (*f*,*g*) Snapshots of the wave pattern at $t = 4.5 \times 10^4$ and 9.0×10^4 s, respectively, in the mBL equation with x-dependent topography $b(x)$ shown under panel (*g*). (*h*,*i*) Interface fluctuations at $t = 9.0 \times 10^4$ s along section lines $y = 0$ and $y = 40$ km, respectively. For the results of the mBL equation with topography $b(x)$, the actual computational domain in the x-direction is twice that shown in the figure to allow for periodicity.

contrast to the KP equation. However, the corresponding group velocities are given by

$$\left.\begin{aligned} \nabla\omega &= \left(-\left(3\vartheta k_x^2 + \frac{c}{2}\frac{k_y^2}{k_x^2}\right) + c,\ \frac{ck_y}{k_x}\right) \quad \text{for the KP equation,} \\ \nabla\omega &= \left(\frac{ck_x}{|\boldsymbol{k}|\left(1+\alpha|\boldsymbol{k}|^2\right)^{3/2}},\ \frac{ck_y}{|\boldsymbol{k}|\left(1+\alpha|\boldsymbol{k}|^2\right)^{3/2}}\right) \quad \text{for the mBL equation.} \end{aligned}\right\} \tag{5.2}$$

https://doi.org/10.1017/jfm.2022.60 Published online by Cambridge University Press

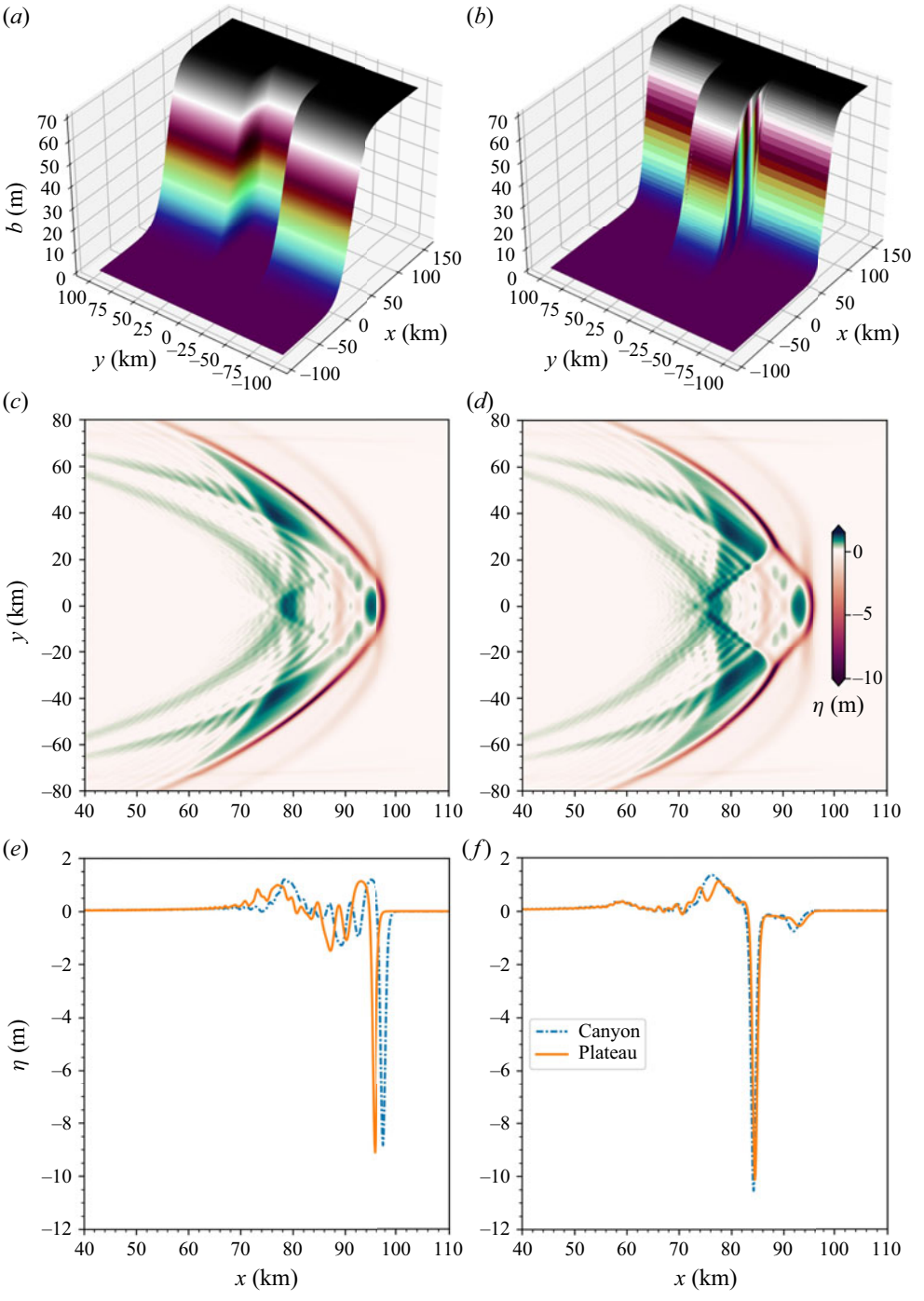

Figure 16. Initial waves, the same as those in figure 13(*a*), evolve over the shoaling topography superposed by bottom canyon (*a*) and plateau (*b*). (*c*,*d*) Snapshots of horizontal wave patterns at time $t = 9.0 \times 10^4$ s over canyon- and plateau-type topographies. (*e*,*f*) Interface fluctuations at $t = 9.0 \times 10^4$ s along section lines $y = 0$ and $y = 40$ km.

https://doi.org/10.1017/jfm.2022.60 Published online by Cambridge University Press

It follows that long waves in the KP equation always propagate towards the positive x-direction considering $k_y \ll k_x \ll 1$; however, there is no preferred direction of propagation for the mBL equation.

The advantage of the mBL equation over the KP equation is confirmed by the results of the MITgcm model, which solves the full Navier–Stokes equations and has been extensively used to simulate internal waves in a realistic oceanic environment; see Vlasenko, Guo & Stashchuk (2012) amongst many others. The fact that the stratification in the ocean is continuous inspires us to propose a layering scheme to allow the mBL equation derived in the two-layer fluid to model internal waves in a continuous stratification, at least in the sense of kinematical equivalence. This is achieved by matching the primary parameters of the KP equation derived from the mBL equation with those of the KP equation related to a continuous stratification. Note that this layering scheme is of practical interest. However, we should caution that any attempt to approximate a continuous stratification by two-layer configuration raises concern about the possible energy transfer among internal gravity modes, which is absent in the two-layer system with the rigid-lid approximation. Moreover, a vortex sheet between successive layers incurred by the layering scheme is inevitable, and thus an evaluation on the influence of this deceptive vortex needs to be conducted.

Although oblique internal wave–wave interactions frequently occur in oceans, few studies were focused on this topic. In the present paper, following the previous work on V-shaped internal solitons (Yuan *et al.* 2018*a*), another type of oblique soliton interaction, the evolution of an initial X-shaped pattern, has been thoroughly investigated. Unlike the diffraction of a truncated solitary wave and the evolution of a partially bent solitary wave, the oblique interactions of X-shaped internal waves show a similarity between the mBL equation and the KP equation, and no perceptible disparities emerge except for slight differences in amplitude. It is striking that the KP equation does an excellent job of describing the dynamics, which may be attributed to the particularity of the problem under study, limiting the free propagation of waves in the y-direction. In reality, the evolution can be classified into three regimes by the amplitudes and inclination angles of the two branches, where peculiar patterns have been presented, for instance, phase shifts and generation of the trapezium. However, when waves are allowed to propagate freely in the y-direction, which simulates internal waves in the open ocean, the aforementioned peculiar wave patterns are thoroughly disrupted. Instead, a leading wave is followed by two curved trailing branches between which there exist wave trains of opposite polarity. Moreover, in these scenarios, the discrepancies between the KP equation and the mBL equation are conspicuous, and the topographic effects become significant in modulating the wave evolution.

In this paper, we modify the classic Benney–Luke equation by including topographic effects. In the derivation, the topography is assumed to be of the same order as the wave amplitude. Hinging on this premise, we point out that the shoaling topography and the topography with transverse variations can decrease the wave speed, augment the wave amplitude and modulate the waveform. Nonetheless, a large amount of observational data imply that large topography can modulate wave propagation to a large extent. This scenario is excluded from the present paper owing to the smallness assumption on bottom topography in the mBL equation. The effects of large topography on internal wave propagation are of great interest and merit further exploration. In addition, Shimizu & Nakayama (2017) studied the effects of the Earth's rotation and undersea topography on oblique interactions between internal solitary waves in the Andaman Sea. They found that the Earth's rotation has little impact on oblique wave–wave interactions. Considering the low latitude ($\sim 9^\circ$N) they investigated, their work inspires us to explore further the

https://doi.org/10.1017/jfm.2022.60 Published online by Cambridge University Press

influence of the Earth's rotation at high latitudes, say the South China Sea (∼22°N), one of the hot-spot regions for studying internal waves, or even the Weddell Sea (∼75°S), as shown by Robertson (2001).

Funding. This work was supported by the National Natural Science Foundation of China (Nos. 11911530171, 11772341, 42006016), the key program of the National Natural Science Foundation of China (Nos. 12132018, 91958206), the Strategic Priority Research Program of the Chinese Academy of Sciences (No. XDB22040203), the Natural Science Foundation of Shandong Province (No. ZR2020QD063) and the China Postdoctoral Science Foundation (No. 2019M660167).

Declaration of interests. The authors report no conflict of interest.

Author ORCIDs.
Chunxin Yuan https://orcid.org/0000-0002-7127-811X;
Zhan Wang https://orcid.org/0000-0003-4393-2118.

References

Ablowitz, M.J. & Baldwin, D.E. 2012 Nonlinear shallow ocean-wave soliton interactions on flat beaches. *Phys. Rev.* E **86**, 036305.

Benjamin, T.B. & Bridges, T.J. 1997 Reappraisal of the Kelvin–Helmholtz problem. Part 1. Hamiltonian structure. *J. Fluid Mech.* **333**, 301–325.

Benney, D.J. & Luke, J.C. 1964 On the interactions of permanent waves of finite amplitude. *J. Math. Phys. (Journal of Mathematical Physics)* **43**, 309–313.

Biondini, G. & Pelinovsky, D. 2008 Kadomtsev–Petviashvili equation. *Scholarpedia* **3** (10), 6539.

Camassa, R., Choi, W., Michallet, H., Rusås, P.-O. & Sveen, J.K. 2006 On the realm of validity of strongly nonlinear asymptotic approximations for internal waves. *J. Fluid Mech.* **549**, 1–23.

Chakravarty, S. & Kodama, Y. 2008 Classification of the line-soliton solutions of KPII. *J. Phys.* A **41**, 275209.

Chakravarty, S. & Kodama, Y. 2009 Soliton solutions of the KP equation and application to shallow water waves. *Stud. Appl. Maths* **123**, 83–151.

Chakravarty, S. & Kodama, Y. 2013 Construction of KP solitons from wave patterns. *J. Phys.* A **47**, 025201.

Chen, Y. & Philip, L.-F. 1995 The unified Kadomtsev–Petviashvili equation for interfacial waves. *J. Fluid Mech.* **288**, 383–408.

Choi, W. & Camassa, R. 1996 Weakly nonlinear internal waves in a two-fluid system. *J. Fluid Mech.* **386**, 1–36.

Choi, W. & Camassa, R. 1999 Fully nonlinear internal waves in a two-fluid system. *J. Fluid Mech.* **313**, 83–103.

Craig, W., Guyenne, P., Nicholls, D.P. & Sulem, C. 2005 Hamiltonian long-wave expansions for water waves over a rough bottom. *Proc. R. Soc. Lond.* A **461**, 839–873.

Craig, W., Schanz, U. & Sulem, C. 1997 The modulational regime of three-dimensional water waves and the Davey–Stewartson system. *Annales de I'I.H.P. Analyse non linéaire* **14** (5), 615–667.

Funakoshi, M. 1980 Reflection of obliquely incident solitary waves. *J. Phys. Soc. Japan* **49**, 2371–2379.

Grimshaw, R. & Melville, W.K. 1989 On the derivation of the modified Kadomtsev–Petviashvili equation. *Stud. Appl. Maths* **80** (3), 183–202.

Guyenne, P. & Nicholls, D.P. 2008 A high-order spectral method for nonlinear water waves over moving bottom topography. *SIAM J. Sci. Comput.* **30** (1), 81–101.

Helfrich, K.R. & Melville, W.K. 2006 Long nonlinear internal waves. *Annu. Rev. Fluid Mech.* **38**, 395–425.

Hsu, M.-K., Liu, A.K. & Liu, C. 2000 A study of internal waves in the China Seas and Yellow Seas using SAR. *Cont. Shelf Res.* **20**, 389–410.

Johnson, R.S. 1982 On the oblique interaction of a large and a small solitary wave. *J. Fluid Mech.* **120**, 49–70.

Kadomtsev, B.B. & Petviashvili, V.I. 1970 On the stability of solitary waves in weakly dispersive media. *Sov. Phys. Dokl.* **15**, 539–541.

Kao, C. & Kodama, Y. 2012 Numerical study of the KP equation for non-periodic waves. *Maths Comput. Simul.* **82**, 1185–1218.

https://doi.org/10.1017/jfm.2022.60 Published online by Cambridge University Press

LI, W., YEH, H. & KODAMA, Y. 2011 On the Mach reflection of a solitary wave: revisited. *J. Fluid Mech.* **672**, 326–357.

MARSHALL, J., ADCROFT, A., HILL, C., PERELMAN, L. & HEISEY, C. 1997 A finite-volume, incompressible Navier Stokes model for studies of the ocean on parallel computers. *J. Geophys. Res.* **102** (C3), 5753–5766.

MELVILLE, W. 1980 On the Mach reflexion of a solitary wave. *J. Fluid Mech.* **98** (2), 285–297.

MILES, J.W. 1977*a* Obliquely interacting solitary waves. *J. Fluid Mech.* **79**, 157–169.

MILES, J.W. 1977*b* Resonantly interacting solitary waves. *J. Fluid Mech.* **79**, 171–179.

MILEWSKI, P.A. & TABAK, E.G. 1999 A pseudo-spectral procedure for the solution of nonlinear wave equations with examples from free-surface flows. *SIAM J. Sci. Comput.* **21** (3), 1102–1114.

NAKAYAMA, K., KAKINUMA, T. & TSUJI, H. 2019 Oblique reflection of large internal solitary waves in a two-layer fluid. *Eur. J. Mech. (*B*/Fluids)* **74**, 81–91.

PERROUD, P.H. 1957 The solitary wave reflection along a straight vertical wall at oblique incidence. PhD thesis, University of California, Berkeley.

PIERINI, S. 1989 A model for the Alboran Sea internal solitary waves. *J. Phys. Oceanogr.* **19** (6), 755–772.

ROBERTSON, R. 2001 Internal tides and baroclinicity in the southern Weddell Sea: 1. Model description. *J. Geophys. Res.* **106**, 27001–27016.

RYSKAMP, S., MAIDEN, M.D., BIONDINI, G. & HOEFER, M.A. 2021 Evolution of truncated and bent gravity wave soliton: the Mach expansion problem. *J. Fluid Mech.* **909**, A24.

SCHLATTER, P., ADAMS, N.A. & KLEISER, L. 2005 A windowing method for periodic inflow/outflow boundary treatment of non-periodic flows. *J. Comput. Phys.* **206** (2), 505–535.

SHIMIZU, K. & NAKAYAMA, K. 2017 Effects of topography and Earth's rotation on the oblique interaction of internal solitary-like waves in the Andaman Sea. *J. Geophys. Res.: Oceans* **122**, 7449–7465.

TANAKA, M. 1993 Mach reflection of a large-amplitude solitary wave. *J. Fluid Mech.* **248**, 637–661.

VLASENKO, V., SANCHEZ GARRIDO, J.C., STASHCHUK, N., LAFUENTE, J.G. & LOSADA, M. 2009 Three-dimensional evolution of large-amplitude internal waves in the Strait of Gibraltar. *J. Phys. Oceanogr.* **39** (9), 2230–2246.

VLASENKO, V., GUO, C. & STASHCHUK, N. 2012 On the mechanism of A-type and B-type internal solitary wave generation in the northern South China Sea. *Deep-Sea Res. (*I*)* **69**, 100–112.

WUNSCH, C. & FERRARI, R. 2004 Vertical mixing, energy, and the general circulation of the oceans. *Annu. Rev. Fluid Mech.* **36** (1), 281–314.

XUE, J., GRABER, H.C., ROMEISER, R. & LUND, B. 2014 Understanding internal wave-wave interaction patterns observed in satellite images of the Mid-Atlantic Bight. *IEEE Trans. Geosci. Remote Sens.* **52** (6), 3211–3219.

YEH, H. & LI, W. 2014 Laboratory realization of KP-solitons. *J. Phys.: Conf. Ser.* **482**, 012046.

YUAN, C., WANG, Z. & CHEN, X. 2020 The derivation of an isotropic model for internal waves and its application to wave generation. *Ocean Model.* **153**, 101663.

YUAN, C., GRIMSHAW, R., JOHNSON, E. & WANG, Z. 2018*a* Topographic effect on oblique internal wave-wave interactions. *J. Fluid Mech.* **856**, 36–60.

YUAN, C., GRIMSHAW, R., JOHNSON, E. & CHEN, X. 2018*b* The propagation of internal solitary waves over variable topography in a horizontally two-dimensional framework. *J. Phys. Oceanogr.* **48** (2), 283–300.

ZAKHAROV, V.E. & SHABAT, A.B. 1974 A scheme for integrating the nonlinear equations of mathematical physics by the method of the inverse scattering problem. *Funct. Anal. Applics.* **8**, 226–235.

https://doi.org/10.1017/jfm.2022.60 Published online by Cambridge University Press